



Available online at www.sciencedirect.com

ScienceDirect

Geochimica et Cosmochimica Acta 330 (2022) 47-66

Geochimica et Cosmochimica Acta

www.elsevier.com/locate/gca

Energetics of hydroxylbastnäsite solid solutions, La_{1-x}Nd_xCO₃OH

Vitaliy G. Goncharov ^{a,b,c,d}, Haylea Nisbet ^a, Andrew Strzelecki ^{b,c,d}, Chris J. Benmore ^e, Artaches A. Migdisov ^a, Hongwu Xu ^{a,f,*}, Xiaofeng Guo ^{b,c,d,*}

^a Earth and Environmental Sciences Division, Los Alamos National Laboratory, Los Alamos, NM 87545, United States
 ^b Department of Chemistry, Washington State University, Pullman, WA 99164, United States
 ^c Alexandra Navrotsky Institute for Experimental Thermodynamics, Washington State University, Pullman, WA 99164, United States
 ^d Materials Science and Engineering Program, Washington State University, Pullman, WA 99164, United States
 ^e Advanced Photon Source, Argonne National Laboratory, Argonne, IL 60439, United States
 ^f School of Molecular Sciences and Center for Materials of the Universe, Arizona State University, Tempe, AZ 85287, United States

Received 30 May 2021; accepted in revised form 3 April 2022; Available online 9 April 2022

Abstract

Bastnäsites (LnCO₃(F,OH)) are a group of common rare earth elements (REE)-bearing minerals and are one of the primary global sources of REE. Due to the chemical similarities among REE, bastnäsites tend to occur as solid solutions instead of end members in REE containing ores. To better understand the processes and the mechanisms of formation of such deposits, it is essential to determine the thermodynamic properties of bastnäsites, including hydroxylbastnäsite (LnCO₃OH) solid solutions. In this work, we performed detailed structural and calorimetric investigations on synthetic hexagonal La-Nd hydroxylbastnäsite ($La_{1-x}Nd_xCO_3OH$, $x_-=0$, 0.25, 0.5, 0.75, 1) solid solutions. X-ray diffraction confirms the crystal structure of the solid solution series in the P6 space group, and pair distribution function (PDF) analysis reveals local bonding environments characterized by three different types of 9-coordinated metal-oxygen polyhedra. Unit cell parameters of $La_{1-x}Nd_xCO_3OH$ exhibit a nearly linear relation with the Nd content x, suggesting a random distribution of La and Nd in the structure. Their standard enthalpies of formation (ΔH_i^c) were determined by high temperature oxide melt drop solution calorimetry, from which the enthalpies of mixing (ΔH_{mix}) were derived. The ΔH_{mix} can be fitted by a regular solution model with an interaction parameter of 12.58 ± 0.16 kJ/mol, suggesting enthalpic metastability of $La_{1-x}Nd_xCO_3OH$ relative to the two endmembers. Combining entropy and enthalpy, we further estimated the Gibbs free energies of mixing (ΔG_{mix}) at relevant temperatures, revealing favorable temperatures under which the intermediate La_{1-x}Nd_xCO₃OH phases can be stabilized. Such entropy-driven stabilization, as is consistent with our geochemical modeling results, may explain the enhancement of thermal stability of the solid solutions in nature. Additionally, the temperature range constrained from this study may be used to estimate the thermal history of REE bastnäsite deposit. © 2022 Elsevier Ltd. All rights reserved.

Keywords: Hydroxylbastnäsite; Solid solution; Enthalpy of mixing; Configurational entropy; Thermal decomposition; Rare earth elements

1. INTRODUCTION

Rare earth elements (REE), including lanthanides (Ln) and Y, are of critical importance to the economy, renewable energy, and national security as they are vital components of many modern technologies such as phosphors, magnets,

^{*} Corresponding authors at: Department of Chemistry, Washington State University, Pullman, WA 99164, United States (X. Guo).

E-mail addresses: hxu@lanl.gov (H. Xu), x.guo@wsu.edu (X. Guo).

electronics, catalysts, and ceramics (Adachi and Imanaka, 1998; Kagan, 2002; Hedrick, 2006; Gschneider et al., 2011; Gschneidner, 2011; McLellan et al., 2013; Pathak et al., 2015). This has led to a nearly exponential global increase in the demand of REE containing ores over the last 70 years (Zhou et al., 2017). Although REE are relatively abundant in the Earth's upper crust (a total average concentration of 169.14 ppm) (Rudnick and Gao, 2003; Zhou et al., 2017), concentrations of individual elements are highly variable. In general, the light rare earth elements (LREE: La-Gd), such as La and Ce (31 ppm and 63 ppm respectively), are considerably more abundant than heavy rare earth elements (HREE: Tb-Lu), such as Tm and Lu (0.30 ppm and 0.31 ppm respectively) (Lide, 2004; Long et al., 2010). Despite their relative abundance, the tendency for REE to concentrate in economically feasible quantities for extraction is rare (Zhou et al., 2017). In addition, due to similarities in their ionic radii in trivalent oxidation states (REE³⁺) (Peters et al., 2020), the majority of REE minerals (e.g., bastnäsite, monazite, xenotime) are found as solid solutions. Therefore, chemistry structures and thermodynamics governing how the REE mix in the solid state plays an important role in controlling the formation and fractionation of REE in natural systems (Gramaccioli et al., 1999; Smith et al., 2000).

While there are more than 200 known REE containing minerals (Kanazawa and Kamitani, 2006; Goodenough et al., 2016), the majority of global REE supply comes from mining and processing four primary minerals: bastnäsite, monazite, xenotime, and loparite (Zhou et al., 2017; Anon, 2020). In the United States, the carbonatite hosted deposits of Mountain Pass are some the most developed sources of LREE in North America, where bastnäsite is the primary ore mineral. (Castor, 2008; Long et al., 2012; Xie et al., 2016). Both the Bayan Obo (Fan et al., 2016) and Maoniuping (Wang et al., 2001) deposits of China, are rich in bastnäsite and represent the current largest accessible REE sources in the world (Zhou et al., 2017). With a large portion of the global supplies of REE tied to bastnäsite (Williams-Jones and Wood, 1992; Schulz et al., 2019), it is imperative to develop a greater understanding of the physical and chemical properties of bastnäsite minerals. This will enable the development of more sophisticated and accurate generic models to better predict REE fractionation (Gysi and Williams-Jones, 2015; Migdisov et al., 2019; Schulz et al., 2019), ultimately enabling improved recovery margins.

Bastnäsites have a general chemical formula of Ln(CO₃) (OH⁻/F⁻), in which Ln are LREE, dominantly La, Ce, Pr, and Nd (Gysi and Williams-Jones, 2015; Shivaramaiah et al., 2016; Kim et al., 2018). Both bastnäsite (hexagonal, P62m and P6) and kozoite (orthorhombic LnCO₃OH, Pnma and P2₁2₁2₁) are thermodynamically stable at ambient and standard conditions (Kim et al., 2018). Although F-containing bastnäsites predominantly occur in nature (Williams-Jones and Wood, 1992; Zhongxin et al., 1992; Castor, 2008; Gysi and Williams-Jones, 2015), the OH-mineral forms LnCO₃OH, hydroxylbastnäsites, comprise an important group of LREE carbonate compounds due to *i*) their marked ambient stability (Rorif et al., 2005;

Vallina et al., 2014; Shivaramaiah et al., 2016; Kim et al., 2018) and ii) being crucial components of the ternary Ln₂O₃ - CO₂ - H₂O system which is often encountered under geochemical conditions that drives Ln carbonate speciation (Rorif et al., 2005; Essington and Mattigod, 1985; Runde et al., 1992; Williams-Jones et al., 2012). Hydroxylbastnäsites also have simpler chemical compositions, which make them easier to synthesize in a laboratory setting for studying both their structural and thermodynamic properties (Szucs et al., 2021). This makes hydroxylbastnäsite an ideal system for systematic investigation of the bastnäsite mineral group, especially F-containing bastnäsites.(Hsu. 1992; Vallina et al., 2014; Kim et al., 2018; Szucs et al., 2021) Ultimately, studying hydroxylbastnäsite has implications towards developing a better prediction of Ln fractionation in natural systems and potential optimization of the Ln mineral extraction process (Cantrell and Byrne, 1987; Schmitt et al., 1991; Williams-Jones and Wood, 1992; Castor, 2008).

To date, there has been significant work on the determination of thermochemical properties of Ln-bearing carbonates end-members (Kim et al., 2018). The effects of heating on morphology of LnCO₃OH have been previously studied (Vallina et al., 2014; Szucs et al., 2021). The enthalpies of formations of several hydroxylbastnäsite and kozoite endmembers have also been measured by calorimetric approaches, where a negative correlation between enthalpy of formation and Ln³⁺ ionic radius was revealed (Rorif et al., 2005; Shivaramaiah et al., 2016; Voigt et al., 2016; Kim et al., 2018). However, ambiguity remains on the thermodynamic stability between hydroxylbastnäsite and kozoite polymorphs. Solubility studies suggest that the hexagonal hydroxylbastnäsites are more stable than their orthorhombic kozoite counterparts (Rorif et al., 2005; Voigt et al., 2016), while the high temperature calorimetric study found the opposite (Shivaramaiah et al., 2016). A recent work by Szucs et al. in 2021 (Szucs et al., 2021) examining the solvent-mediated pseudomorphic mineral replacement of calcite by Ln-carbonates (Ln = La, Nd, Dy) demonstrated the following crystallization sequence occurring at low temperature hydrothermal conditions (50-220 °C): $Ln_2(CO_3)_3 \cdot 8H_2O$ (lanthanite) \rightarrow orth-LnCO₃ OH (kozoite) → hex-LnCO₃OH (hydroxylbastnäsite). Alluding to the increased thermodynamic stability of hydroxylbastnäsite in relation to kozoite at low temperature hydrothermal conditions (Szucs et al., 2021), in agreement temperature calorimetric measurements with high (Shivaramaiah et al., 2016). Although these studies reveal the energetic trend of LnCO₃OH across the lanthanide series, they did not consider thermodynamic effects from mixing of multiple Ln cations in the hydroxylbastnäsite solid solution, which are dominantly occurring in mineral deposits (Maksimović and Pantó, 1985; Williams-Jones and Wood, 1992; Peishan et al., 1995; Schoneveld et al., 2015). These solid solutions may possess synergetic or competing enthalpic and entropic contributions (Guo et al., 2016), which can control phase equilibria of various Ln containing hydroxylbastnäsites (Kim et al., 2018). This, however, requires experimental validations to derive the thermodynamic models of various Ln cations in LnCO₃OH (Christensen, 1973; Maksimović and Pantó, 1985; Williams-Jones and Wood, 1992; Gysi and Williams-Jones, 2015).

Moreover, Ln often function as surrogates for trivalent actinides in geological repositories (Du Fou de Kerdaniel et al., 2007; Guo et al., 2015; Tang et al., 2020; Strzelecki et al., 2020a). For example, Nd3+ has been shown to be an effective analog for Am³⁺ due to their similarities in ionic size, crystallographic behavior, and oxidation state (Carroll, 1993; Meinrath and Takeishi, 1993). Since geological repositories are likely to be located in hard rock below aguifers, gradual incursion of H₂O into the repository (resaturation) is inevitable at time-scales required for the decay of nuclear fission products (Cho et al., 2014). The occurrence of CO₂ within repositories (formed by microbial or inorganic means) (Xiong and Lord, 2008), leads to the formations of low temperature CO₂ - H₂O hydrothermal conditions. Such conditions could have a significant impact on mobilization and transport of actinides with the surrounding environments (Witherspoon, 1991; Meinrath and Takeishi, 1993; Kalintsev et al., 2021; Nisbet et al., 2022). Hydroxylbastnäsites are thermodynamically stable components in the Ln₂O₃ - H₂O - CO₂ equilibrium systems. Thus, thermodynamic knowledge of LnCO₃OH can permit an evaluation of actinide behavior in H₂O - CO₂ environments relevant to geological nuclear waste storage conditions (Ringwood et al., 1979; Ewing et al., 2016).

Therefore, in this work, we systematically investigated both the structures and thermodynamics of hydroxylbastnäsite solid solutions by a combination of synchrotron X-ray diffraction and high temperature calorimetric techniques. Hexagonal $La_{1-x}Nd_xCO_3OH$, x = 0, 0.25, 0.5, 0.75, and 1 (Fig. 1), were synthesized by hydrothermal methods. The crystal structure was determined by performing powdered X-ray diffraction (XRD) and pair distribution function (PDF) analysis. Thermal decomposition of La_{1-x}Nd_xCO₃OH under Ar was examined by thermal gravimetric analysis (TGA) coupled with differential scanning calorimetry (DSC) and evolved gas by mass spectrometry (MS). Finally, high temperature oxide melt drop solution calorimetry was used to determine the enthalpies of formation of La_{1-x}Nd_xCO₃OH solid solutions from elements $(\Delta H^{\circ}_{\rm f})$ and from constituent binary oxides $(\Delta H_{\rm f.ox})$. Enthalpies of mixing (ΔH_{mix}) of La_{1-x}Nd_xCO₃OH were then derived from the experimentally measured drop enthalpy values ($\Delta H_{\rm ds}$). The outcome of this work provides fundamental thermodynamic data for the La_{1-x}Nd_xCO₃OH system and proposes a thermodynamic rationale for hydroxylbastnäsite formation in natural systems. This study serves as the initial step towards future geochemical assessments of REE mineralization and fractionation within the greater bastnäsite mineral group.

2. EXPERIMENTAL METHODS

2.1. Synthesis

Hexagonal hydroxylbastnäsites in the stoichiometric form of $La_{1-x}Nd_xCO_3OH$, x = 0, 0.25, 0.5, 0.75, and 1, were synthesized via a previously reported hydrothermal

method (Vallina et al., 2015). 50 mM solutions of LaCl₃ and NdCl₃ (99.9%, anhydrous, Alfa Aesar) were mixed with 50 mM of a Na₂CO₃ solution by adding appropriate stoichiometric quantities for the desired phases. Immediately, an amorphous REE carbonate phase precipitated out of solution (Vallina et al., 2015). The resultant slurry was added to Teflon-lined titanium autoclaves and heated at 165 °C in a muffle furnace. The autoclaves were gently shaken every 10 mins for initial 60–100 mins of heating. After 1-14 weeks, the autoclaves were removed from the furnace and allowed to cool. Approximately, 3, 10 and 14 weeks were required for the desired synthesis of LaCO₃OH/NdCO₃OH endmembers, La_{0.25}Nd_{0.75}CO₃OH/ La_{0.75}Nd_{0.25}CO₃OH and La_{0.5}Nd_{0.5}CO₃OH, respectively. Next, the products were filtered through glass vacuum filters set-up using 2.5 µm filter paper and rinsed several times with deionized water and isopropyl alcohol. The resultant powders were dried at room temperature for 12 hrs.

2.2. Characterization

Powder X-ray diffraction: $La_{1-x}Nd_xCO_3OH$ (x = 0, 0.25,0.5, 1) samples were loaded into Kapton tubes and then transferred to beamline 6-IDD of the Advanced Photon Source (APS), Argonne National Laboratory. The wavelength of the X-ray was set to 0.123696 Å (100.233 keV). Two-dimensional (2D) diffraction images were collected using an amorphous Silicon area detector (Varex CT4343), and the geometric parameters calibrated by a CeO₂ standard. The sample to detector distance was fixed at 344 mm during the experiments. The samples were exposed to the incident X-rays for 10 s (0.01 s \times 1000) to acquire diffraction images with sufficient ring intensities. The obtained 2D diffraction data were corrected for dark current, integrated and calibrated by General Structure Analysis System software version II (GSAS-II) (Toby et al., 2013) to obtain the patterns that are plotted as intensity as a function of Q (\mathring{A}^{-1}) (Fig. S1). Note, as a result of insufficient quantity of sample La_{0.25}Nd_{0.75}CO₃OH at the time of the synchrotron XRD beamtime, we had to use the previous XRD data collected on a laboratory-based X-ray diffractometer (Bruker D8 Discover X-ray Diffractometer). The diffractometer used Cu $K\alpha_{1,2}$ radiation $(\lambda = 1.54184 \text{ Å})$ and was equipped with a LynxEye position sensitive detector. The PXRD data were collected for approximately 1 hour in the range of $5^{\circ} < 2\theta < 70^{\circ}$ or $0.36 \text{ Å}^{-1} \le Q \le 4.68 \text{ Å}^{-1}$. All diffraction patterns were analyzed by the Rietveld method with GSAS-II, where the instrument parameters were fixed at those obtained by the fitted diffraction peaks of CeO₂, the background by Chebyshev function (8 terms), and the peak profiles to pseudo-Voigt convolution functions (Thompson et al., 1987). The Rietveld refinements were performed to determine the crystal structures with $R_{\rm wp}$ ranging from 5.6% to 10.0% for high-energy XRD and 15.3% for lab-based XRD (Table 1). In additional, the pair distribution function (PDF) of X-ray scattering data was fitted using PDFgui (Farrow et al., 2007), from which G(r) data were determined and plotted in Fig. S2 in Supporting Information (SI). Such procedures were also stated previously elsewhere (Xu et al., 2017; Guo

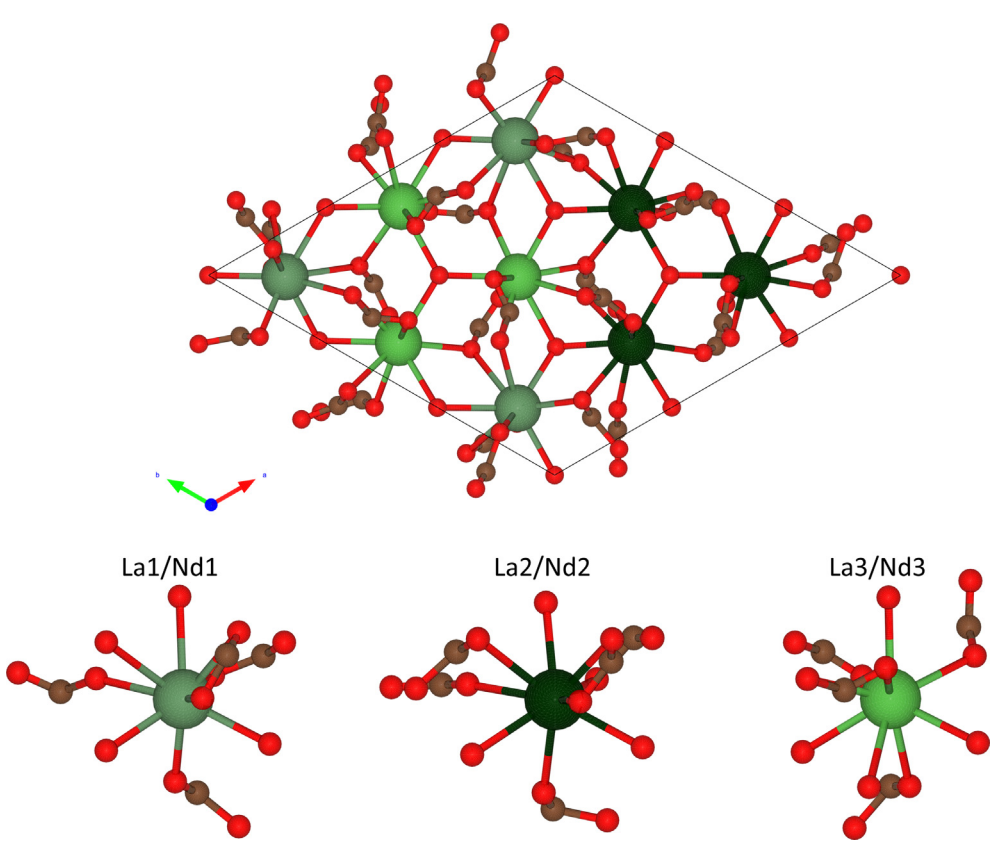


Fig. 1. Top: crystal structure of hexagonal REECO₃OH; bottom: local REE coordination environments obtained from PDF analysis. *Large green* spheres – REE; *small red* spheres – O; *small brown* sphere – C.

Table 1 Summary of unit cell parameters and molar volumes of $La_{1-x}Nd_xCO_3OH$.

Formula	a (Å)	c (Å)	Volume (Å ³)	R _{wp} (%)
LaCO ₃ OH	12.622(4)	10.024(1)	1383.0(5)	5.55
La _{0.75} Nd _{0.25} CO ₃ OH	12.541(4)	9.984(1)	1359.9(5)	6.10
$La_{0.50}Nd_{0.50}CO_{3}OH$	12.450(8)	9.947(2)	1332.0(10)	6.63
La _{0.25} Nd _{0.75} CO ₃ OH	12.398(5)	9.925(1)	1321.2(6)	15.31
NdCO ₃ OH	12.351(2)	9.895(2)	1307.2(3)	7.38

et al., 2019b; Strzelecki et al., 2020b; Strzelecki et al., 2021; Marcial et al., 2021).

X-ray fluorescence: Chemical compositions and impurities of samples were examined by using a Bruker S2 PICO-FOX benchtop total reflection X-ray fluorescence (TXRF) spectrometer equipped with an air-cooled molybdenum X-ray source of 50 kV (Bruker Nano GmbH, 2010a). The instruments gain correction and resolution were calibrated prior to each series of measurements. Reusable quartz discs $(3 \times 30 \text{ mm})$ were employed for all measurements. No addition of an internal standard was added in this method. Measurements were collected while operating in "standardless mode" with the blank value being 0%. Each individual measurement had an acquisition time of 600 seconds. The spectra were preliminarily processed by Spectra 7 software using optimized Bayes fit technique (Bruker Nano GmbH, 2010b). Use of the Hephaestus database (Ravel and Newville, 2005) was ultimately employed in order to correctly assign the peaks presented in the XRF spectra to the appropriate fluorescence emission lines.

2.3. Thermodynamic investigations

Thermal analysis: Thermogravimetric analysis and differential scanning calorimetry (TGA-DSC) of $La_{1-x}Nd_x$ -CO₃OH was conducted simultaneously on a TA Instrument Q600 SDT thermal analyzer with a heating rate of 10 °C/min to 900 °C in a flow of ultrapure Argon (60 mL/min). The identities of evolved gases during thermal decomposition of $La_{1-x}Nd_xCO_3OH$ were determined *in situ* by mass spectrometry (Discovery MS, TA Instruments). The sensitivity of the calorimeter was calibrated using the thermal decomposition of CaC_2O_4 and melting cycles of various metals, full description of which may be found elsewhere (Guo et al., 2014b; Olds et al., 2020; Strzelecki et al., 2020b).

High temperature oxide melt drop solution calorimetry: High temperature thermochemical experiments were preformed utilizing a Calvet-type twin microcalorimeter (AlexSYS - 800) at LANL (Xu et al., 2015; Guo and Xu, 2017; Guo et al., 2018; Chung et al., 2019; Guo et al., 2019a). Dried powdered samples were pressed into ~ 5 mg pellets using a hand die. Pellets were then dropped from room temperature into the molten sodium molybdate (3NaO·4MoO₃) solvent (~15 g) contained within quartz crucibles at 700 °C. A total of eight drops (four per side) were conducted per an experimental set up. O₂ gas was continuously flushed through the calorimetric chamber at 120 mL/min to maintain a constant gas environment over the solvent (Navrotsky et al., 1994). Upon the dissolution of La_{1-x}Nd_xCO₃OH pellets in the solvent, the enthalpy of drop solution (ΔH_{ds}) was obtained. The complete dissolution of trivalent Ln compounds has been previously confirmed in molten 3NaO-4MoO3 solvent allowing effective determination of ΔH_{ds} values (Ushakov et al., 2001; Zhang and Navrotsky, 2004; Cheng et al., 2005; Guo et al., 2014a; Guo et al., 2015; Qi et al., 2015; Strzelecki et al., 2020a; Strzelecki et al., 2020b). Instrument calibration procedures and in-depth descriptions of the calorimetric methodologies may be found in previous reports (Navrotsky, 2014; Guo et al., 2019a; Voskanyan et al., 2020).

Thermodynamic calculation for geochemical equilibrium modeling: The calculations were performed using Hch/Unitherm code (Shvarov and Bastrakov, 1999; Shvarov, 2010). The models used here were designed to evaluate the stability field of La_{1-x}Nd_xCO₃OH as a function of temperature from room temperature to 450 °C, where the regular solution model determined from calorimetry was used. In highly simplified hypothetical geochemical scenarios, we have the following solid phases to be evaluated: LaCO₃OH, NdCO₃OH, and two solid solutions La_{1-x}Nd_xCO₃OH, from reaction of NaHCO₃ and LaCl₃/NdCl₃ aqueous solutions. Due to the lack of the thermodynamic parameters of

Ln containing phases, determination of their estimate values was discussed in SI. Results of Hch/Unitherm modeling are deposited in *Research Data*.

3. RESULTS

LaCO₃OH and NdCO₃OH were analyzed for elemental purity via TXRF (Figs. S3 and S4). Due to the use of quartz discs for a sample substrate and silicone-based vacuum grease as an adhesion material, both spectra have a peak located at 1.74 keV, and are assigned to Si $K\alpha_{1,2}$. In addition, each spectrum has a peak located 2.96 keV (Ar argon $K\alpha_{1,2}$), corresponding to atmospheric argon. All other peaks are diagnostic of the elemental composition of the sample. For the TXRF spectrum of LaCO₃OH (Fig. S3), all sample-related peaks can be assigned to La. However, the spectrum of NdCO₃OH presented in Fig. S4 contains a single peak attributed to La $L\alpha_2$. Such impurity is a possible residual La in the synthesis reagent (NdCl₃) or a presence of minor La contamination on the TXRF sample holder (quartz disc). The quantification of La by the Spectra 7 TXRF software (Bruker Nano GmbH, 2010b) indicated less than 0.4 mol % La, which was not expected to significantly influence the enthalpic signature of NdCO₃OH (influence of possible contamination falls within the measurement uncertainty).

The XRD patterns (Figs. 2 and S1) indicate that synthesized $La_{1-x}Nd_xCO_3OH$ solid solutions and endmembers are all single phases (space group P 6) belonging to $LaCO_3OH$, $La_{0.75}Nd_{0.25}CO_3OH$, $La_{0.5}Nd_{0.5}CO_3OH$, $La_{0.25}Nd_{0.75}CO_3OH$, and $NdCO_3OH$ as determined by stoichiometric metal ratios of precursors used in the synthesis (Vallina et al., 2014; Shivaramaiah et al., 2016). The refined unit cell parameters and molar volumes are given in Table 1 and plotted in Fig. 3. The unit cell parameters a and c of $La_{1-x}Nd_xCO_3OH$ solid solution endmembers (Table 1) are in general agreement with those previously determined for

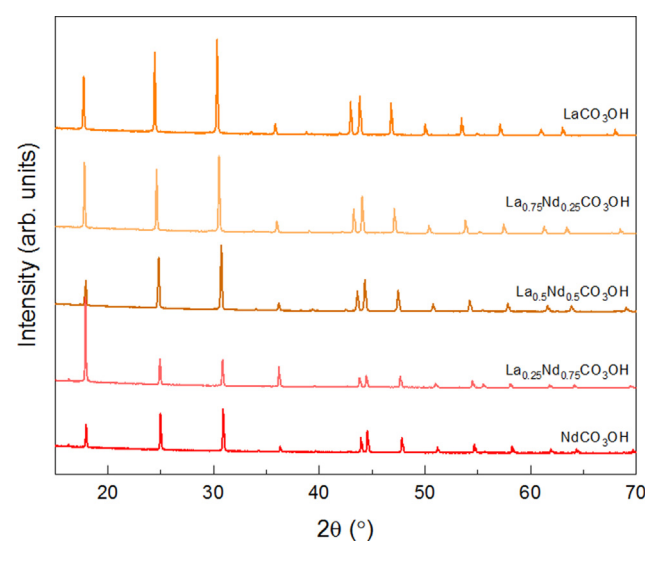


Fig. 2. XRD patterns of $La_{1-x}Nd_xCO_3OH$ solid solutions. All samples are phase pure and have XRD peaks consistent with the hexagonal P 6 space group.

the hexagonal polymorphs of LaCO₃OH and NdCO₃OH (Michiba et al., 2011; Shivaramaiah et al., 2016; Kim et al., 2018).

The results of TGA–DSC–MS experiments conducted up to 900 °C under Ar are shown in Fig. 4 and summarized in Table 2. The thermal decompositions of La_{1-x}Nd_xCO₃-OH solid solutions and two endmembers, LaCO₃OH and NdCO₃OH follow the standard decomposition pathway previously reported for dehydrated hydroxylbastnäsites (Kim et al., 2018).

High temperature oxide melt drop solution calorimetry was conducted on the dried as-synthesized samples to directly measure the enthalpy of drop solution ($\Delta H_{\rm ds}$) of each La_{1-x}Nd_xCO₃OH sample. $\Delta H_{\rm ds}$ values were then used in thermochemical cycles (Table 3), in combination with other reference $\Delta H_{\rm ds}$ values and auxiliary data, to derive the enthalpy of mixing ($\Delta H_{\rm mix}$), the enthalpy of formation from constituent oxides ($\Delta H_{\rm f,ox}$), and the standard enthalpy of formation from the elements ($\Delta H^{\circ}_{\rm f}$) (Table 4).

4. DISCUSSION

4.1. Chemical and crystallographic analyses

Both of the unit cell parameter a and c were found to exhibit a nearly linear decrease with increasing Nd concentration (Fig. 3a). For the a unit cell parameter this was to occur from 12.622 Å (LaCO₃OH) to 12.351 Å (NdCO₃OH), while the unit cell parameter c was from 10.024 Å (LaCO₃OH) to 9.895 Å (NdCO₃OH). The reduction in the unit cell parameters upon substitution of La by Nd primarily arises from the smaller ionic radius of Nd³⁺ (1.163 Å) compared to La³⁺ (1.216 Å). However, the reduction in unit cell parameters was found to occur anisotropically as a parameter decreases \sim 2.1 % as function of Nd content, while the c parameter decreases only \sim 1.3% as a function of Nd content. Moreover, the PDF analysis from the X-ray total scattering data resolved the first coordination shells of La- or Nd-centered polyhedra. Three different

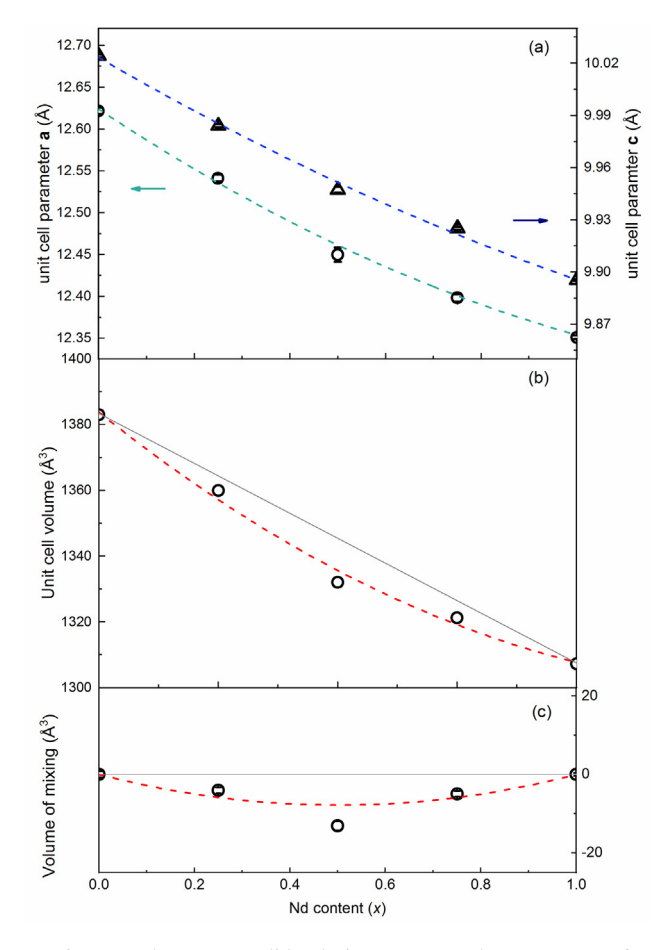


Fig. 3. Refined unit cell parameters of La_{1-x}Nd_xCO₃OH solid solutions: (a) a and c parameters fitted to equations (12.624 \pm 0.005) + (-0.38 \pm 0.03)·x + (0.10 \pm 0.03)· x^2 (adjusted R^2 = 0.9982), and (10.023 \pm 0.003) + (-0.16 \pm 0.02)·x + (0.03 \pm 0.01)· x^2 (adjusted R^2 = 0.9981), respectively. Circles and triangles represent the a and c parameters respectively, with arrows denoting each to the appropriate numerical axis (a parameter left, and c parameter right); (b) cell volume V_{cell} fitted by Eq. (1) with an adjusted R^2 = 0.9854; (c) volume of mixing ΔV_{mix} fitted by equation ΔV_{mix} = (-31 \pm 6)·x(1 - x) Å³, with an adjusted R^2 = 0.8095.

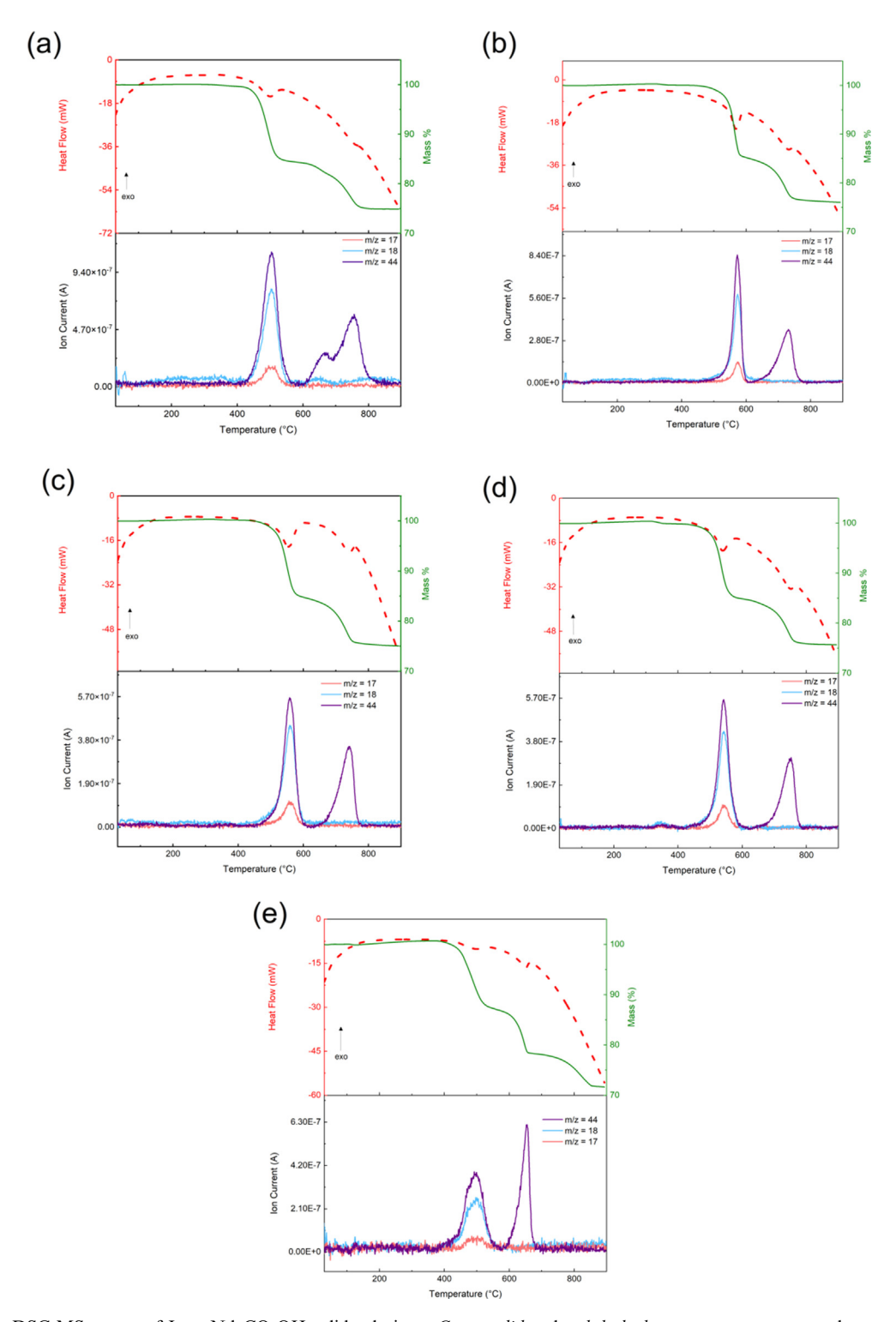


Fig. 4. TGA-DSC-MS curves of $La_{1-x}Nd_xCO_3OH$ solid solutions. Green solid and red dashed curves represent mass change and heat flow signals, respectively. The primary MS signals detected during the thermal decompositions are m/z = 44, m/z = 18 and m/z = 17 corresponding to CO₂, H₂O, and OH, respectively. (a) LaCO₃OH. (b) La_{0.75}Nd_{0.25}CO₃OH. (c) La_{0.5}Nd_{0.5}CO₃OH. (d) La_{0.25}Nd_{0.75}CO₃OH. (e) NdCO₃OH.

9-coordinated metal polyhedra were identified (Fig. 1), each coordinated with three monodentate and one bidentate carbonate ligands, and three more oxygen connected to other type metal cations. This local structure is consistent with

the crystal structure proposed by Michiba et al. (Michiba et al., 2011) while deviating from earlier works (Christensen, 1973; Kutlu and Meyer, 1999). In comparison, the monoclinic La_{1-x}Nd_xPO₄ (monazite, space group

Table 2
TGA results of La_{1-x}Nd_xCO₃OH under Ar correlating experimental and theoretical mass loss % accompanying thermal decomposition.

Decomposition Steps	Temperature (°C)	Experimental Weight loss (%)	Theoretical weight loss (%)	Difference (%)
LaCO ₃ OH → La ₂ O ₂ CO ₃	462	-15.88	-14.36	1.52
$La_2O_2CO_3 \rightarrow La_2O_3$	630	-9.19	-10.19	1.00
$La_{0.75}Nd_{0.25}CO_3OH \rightarrow$	514	-15.87	-14.28	1.59
$(La_{0.75}Nd_{0.25})_2O_2CO_3$				
$(La_{0.75}Nd_{0.25})_2O_2CO_3 \rightarrow$	697	-8.45	-10.13	1.68
$(La_{0.75}Nd_{0.25})_2O_3$				
$La_{0.5}Nd_{0.5}CO_3OH \rightarrow$	528	-15.72	-14.19	1.53
$(La_{0.5}Nd_{0.5})_2O_2CO_3$				
$(La_{0.5}Nd_{0.5})_2O_2CO_3 \rightarrow (La_{0.5}Nd_{0.5})_2O_3$	705	-9.23	-10.07	0.84
$La_{0.25}Nd_{0.75}CO_3OH \rightarrow$	530	-15.83	-14.10	1.72
$(La_{0.25}Nd_{0.75})_2O_2CO_3$				
$(La_{0.75}Nd_{0.25})_2O_2CO_3 \rightarrow$	685	-8.09	-10.00	1.92
$(La_{0.75}Nd_{0.25})_2O_3$				
$NdCO_3OH \rightarrow Nd_2O_2CO_3$	440	-13.38	-14.02	0.64
$Nd_2O_2CO_3 \rightarrow Nd_2O_3$	615	-9.02	-9.94	0.92

Table 3 Thermochemical cycles for $La_{1-x}Nd_xCO_3OH$ based on high temperature oxide melt drop solution calorimetry in molten $3NaO \cdot 4MoO_3$ solvent at 700 °C.

Reaction	ΔH (kJ/mol)
(1) $\text{La}_{1-x}\text{Nd}_x\text{CO}_3\text{OH}_{(s, 25 ^{\circ}\text{C})} \rightarrow (1-x)/2 \text{La}_2\text{O}_{3 (sln, 700 ^{\circ}\text{C})}$	$\Delta H_1 = \Delta H_{ m ds}^*$
$+ x/2 \text{ Nd}_2\text{O}_3 \frac{1}{(\text{sln}, 700 ^{\circ}\text{C})} + 1/2 \text{ H}_2\text{O} \frac{1}{(\text{g}, 700 ^{\circ}\text{C})} + \text{CO}_2 \frac{1}{(\text{g}, 700 ^{\circ}\text{C})}$	
(2) $H_2O_{(l, 25 °C)} \rightarrow H_2O_{(g, 700 °C)}$	$\Delta H_2 = 69.00$
	(Chase, 1998)
(3) $CO_{2 (g, 25 \circ C)} \rightarrow CO_{2 (g, 700 \circ C)}$	$\Delta H_3 = 31.95$
	(Chase, 1998)
(4) $La_2O_{3 (s, 25)} \circ_{C)} \rightarrow La_2O_{3 (sln, 700)} \circ_{C)}$	$\Delta H_4 = -225.10 \pm 3.16$
	(Cheng et al., 2005)
(5) Nd_2O_3 (s, 25 °C) $\rightarrow Nd_2O_3$ (sln, 700 °C)	$\Delta H_5 = -163.36 \pm 3.44$
	(Ushakov et al., 2001)
(6) $3/2 O_{2 (g, 25)} C_{)} + 2 La_{(s, 25)} C_{)} \rightarrow La_{2}O_{3 (s, 25)} C_{)}$	$\Delta H_6 = -1791.6 \pm 2.0$
	(Konings et al., 2014)
(7) $H_{2 (g, 25 \circ C)} + 1/2 O_{2 (g, 25 \circ C)} \rightarrow H_{2}O_{(l, 25 \circ C)}$	$\Delta H_7 = -285.83$
	(Chase, 1998)
(8) $O_{2 (g, 25 \circ C)} + C_{(s, 25 \circ C)} \rightarrow CO_{2 (g, 25 \circ C)}$	$\Delta H_8 = -393.52$
(2) 4/4 (2)	(Chase, 1998)
(9) $3/2 O_{2 (g, 25 ^{\circ}C)} + 2 Nd_{(s, 25 ^{\circ}C)} \rightarrow Nd_{2}O_{3 (s, 25 ^{\circ}C)}$	$\Delta H_9 = -1807.95 \pm 0.92$
	(Fitzgibbon et al., 1968)
Enthalpy of mixing of $La_{1-x}Nd_xCO_3OH$ from $LaCO_3OH$ and $NdCO_3OH$	
$\Delta H_{\text{mix}}(\text{La}_{1-x}\text{Nd}_x\text{CO}_3\text{OH}) = -\Delta H_1 + (1-x) \Delta H_{\text{ds}}(\text{LaCO}_3\text{OH})^* + x \Delta H_{\text{ds}}(\text{NdCO}_3\text{OH})^*$	
Enthalpy of formation of $La_{1-x}Nd_xCO_3OH$ from La_2O_3 , Nd_2O_3 , H_2O , and CO_2 at 25 °C	
$\Delta H_{f,ox}(\text{La}_{1-x}\text{Nd}_x\text{CO}_3\text{OH}) = -\Delta H_1 + \frac{1}{2}\Delta H_2 + \Delta H_3 + (1-x)/2\Delta H_4 + \frac{x}{2}\Delta H_5$ Some distribution of formation of f and f and f and f and f and f and f are f formation of f and f and f are f formation of f are f formation of f and f are f formation of f are f formation of f and f are f formation of f and f are f formation of f and f are f formation of f are f and f are f are f are f are f and f are f are f are f and f are f are f are f are f and f are f are f are f and f are f are f are f are f and f are f are f are f and f are	
Standard enthalpy of formation of $La_{1-x}Nd_xCO_3OH$	
$\Delta H_{\text{f}}^{\circ} (\text{La}_{1-x} \text{Nd}_{x} \text{CO}_{3} \text{OH}) = \Delta H_{\text{f,ox}} + (1-x)/2 \Delta H_{6} + \frac{1}{2} \Delta H_{7} + \Delta H_{8} + \frac{x}{2} \Delta H_{9}$	

^{*} Experimentally measured in this work and presented in Table 4.

 $P2_1/n$) solid solution has linear decreases in the unit cell parameters with increasing Nd content (Schlenz et al., 2019). Similar trends have been observed for other LnPO₄ solid solutions (Clavier et al., 2011; Heuser et al., 2018; Zaman and Antao, 2020).

The findings of the anisotropic contraction of the a and c unit cell parameters are likely attributed to other inherent structural effects of the system (Michiba et al., 2011; Shivaramaiah et al., 2016). Recent work (Shivaramaiah et al., 2016) suggested that the hexagonal hydroxyl-

bastnäsites have a similar sublattice for OH⁻, but not isostructural to that of F⁻ in the fluoride-bastnäsite counterparts. The major difference arises from the orientation of the OH⁻/F⁻ anion in relation to the REE cation-containing plane (Fig. 1). OH⁻ in hexagonal LaCO₃OH and NdCO₃OH are not coplanar to the REE cations (unlike the F⁻ in bastnäsites) and likely to have the ability to form hydrogen bonds with the adjacent oxygens of the carbonate polyhedra (Michiba et al., 2011; Shivaramaiah et al., 2016). Because the hexagonal hydroxylbastnäsite

Table 4 Enthalpies of drop solution ($\Delta H_{\rm ds}$), enthalpies of formation of hexagonal La_{1-x}Nd_xCO₃OH from corresponding oxides ($\Delta H_{\rm f,ox}$), and standard enthalpy of formation ($\Delta H^{\circ}_{\rm f}$).

Sample	$\Delta H_{ m ds}$ (kJ/mol)	$\Delta H_{ m f,ox}$ (kJ/mol)	$\Delta H^{\circ}_{f} (kJ/mol)$
LaCO ₃ OH	$150.91^{\rm a} \pm 1.07^{\rm b}(4)^{\rm c}$	-197.0 ± 1.9	-1629.3 ± 2.2
	$150.57 \pm 0.45*$	-196.6 ± 1.6 *	-1628.8 ± 2.5 *
La _{0.75} Nd _{0.25} CO ₃ OH	$148.45^{\rm a} \pm 0.63^{\rm b}(4)^{\rm c}$	-186.8 ± 1.3	-1621.1 ± 1.5
La _{0.5} Nd _{0.5} CO ₃ OH	$147.29^{a} \pm 0.94^{b}(4)^{c}$	-178.0 ± 1.5	-1614.3 ± 1.6
La _{0.25} Nd _{0.75} CO ₃ OH	$147.94^{a} \pm 0.77^{b}(4)^{c}$	-170.9 ± 1.6	-1609.3 ± 1.6
NdCO ₃ OH	$150.11^{\rm a} \pm 0.48^{\rm b}(4)^{\rm c}$	-165.3 ± 1.8	-1605.8 ± 1.9
	$149.90 \pm 2.52*$	$-165.0 \pm 3.1*$	-1604.9 ± 5.7 *

^a Averaged value.

polymorphs consist of alternating layers of 9-coordinated REE linked by carbonate anions, hydrogen bonding interactions of OH⁻ with adjacent oxygens of the carbonate polyhedra may result in a unique distortion of that polyhedra, leading to complexity of vibrational signatures of hexagonal hydroxylbastnäsites (Michiba et al., 2011; Shivaramaiah et al., 2016). Additionally, if the formations of these hydrogen bond interactions have a directional preference, it could also induce anisotropic behavior in elastic properties of hydroxylbastnäsites (Santos-Martins and Forli, 2020).

As the Nd content increases, the unit cell volume of La_{1-x}Nd_xCO₃OH decreases (~5.4 % from LaCO₃OH to NdCO₃OH), with a slightly negative deviation from Vegard's law (Vegard, 1921; Chai and Navrotsky, 1996), which can be described by Eq. (1):

$$V_{cell} = a + bx + cx^2 \tag{1}$$

where $a = 1383.8 \pm 3.4 \text{ Å}^3$, $b = -116.5 \pm 16.1 \text{ Å}^3$, c = 40. $4 \pm 15.4 \,\text{Å}^3$, and an adjusted $R^2 = 0.9861$ (Fig. 3). Then the volume of mixing is given by $\Delta V_{\text{mix}} = (-31 \pm 6) \cdot x(1-x)$ $Å^3$, and is only slightly negative compared to the large unit cell volumes. A negative deviation of ΔV_{mix} from Vegard's law may be due to: i) local range ordering of mixed cations; ii) difference in bonding character of the mixed cations (Le Tonquesse et al., 2019); iii) distortions of metal polyhedral coordination cites (Chizmeshya et al., 2003; Marcial et al., 2021). Due to the small negativity in linear deviation (\sim 1% of the total unit cell volume) and the similarity in ionic radii, short-range ordering is not expected. Second, the negative volume of mixing of Nd and La in La_{1-x}Nd_xCO₃OH due to the difference of La³⁺ and Nd³⁺ bonding character is also unlikely due to lanthanide contraction, with their coordination behavior largely dictated by ionic radius (Karraker, 1970; Polinski et al., 2012). The slightly negative deviation of ΔV_{mix} is likely explained by the ability of the Ln coordinated OH⁻ groups to form hydrogen bonds with adjacent oxygens leading to slight polyhedral distortions. Due to the presence of three different types of Lncoordination environments (Fig. 1), it is difficult to ascertain the exact role of hydrogen bonding within the La_{1-x}-Nd_xCO₃OH structure. The greater reduction in the unit cell parameter a compared to c (with increasing Nd content) suggests that hydrogen bonding may likely occur along the a direction, parallel to the plane of the 9-coordinant REE-sheets. This may cause the contraction of the lattice (Aakeröy et al., 1992) unaccounted for by the ionic size differences between ${\rm La^{3+}}$ and ${\rm Nd^{3+}}$ and a slightly negative deviation in $\Delta V_{\rm mix}$ from Vegard's law. Thus, we concluded that the mixing of La and Nd follows a near-random distribution in the metal sublattice of ${\rm La_{1-x}Nd_xCO_3OH}$. This implies that the configurational entropy generated from the mixing of La and Nd can be well-approximated by the Boltzmann entropy formula. Although, additional studies such as computationally assisted total neutron scattering (Marcial et al., 2021) are required to validate the origin of the ${\rm La_{1-x}Nd_xCO_3OH}$ slight deviation from Vegard's Law.

4.2. Thermal decomposition and thermal stability

The stepwise thermal decomposition of $La_{1-x}Nd_xCO_3$ -OH in an inert environment is represented by *reactions* (2) and (3):

$$2La_{1-x}Nd_xCO_3OH\rightarrow (La_{1-x}Nd_x)_2O_2CO_3 + CO_2 + H_2O$$
(2)

$$(La_{1-x}Nd_x)_2O_2CO_3 \rightarrow (La_{1-x}Nd_x)_2O_3 + CO_2$$
 (3)

Noted that the intermediate product $(La_{1-x}Nd_x)_2O_2CO_3$ only represents the mass stoichiometry derived from TGA and is not a conclusive determination; and the final product $(La_{1-x}Nd_x)_2O_3$ is assumed to be a sesquioxide solid solution (Collongues, 1992; Schweda and Kang, 2005). The summary of the thermogravimetric analysis and the representative onset temperatures of decomposition reactions are presented in Table 2. Decomposition of $La_{1-x}Nd_xCO_3OH$ via reactions (2) and (3) is well explained by the close agreement between the experimental and theoretical weight loss % determined by TGA and supported by the evolved gas analysis by MS (Fig. 4).

To further evaluate the thermal decomposition process of hexagonal La_{1-x}Nd_xCO₃OH and to attain higher confidence about the onset temperatures of *reactions* (2) and (3), the MS signal of decarbonation (m/z = 44) was further deconvoluted using normal distributions ($R^2 \ge 0.99$,

^b Two standard deviations of the average value.

^c Number of measurements.

^{*} Previously measured by high temperature drop solution calorimetry (Shiyaramaiah et al., 2016).

Figs. S5 - S9), each of which corresponds to step-wise release of CO2 from thermal decarbonation (Head and Holley, 1962; Head and Holley, 1963; D'Assunção et al., 1993). For instance, in the thermal decomposition of LaCO₃OH (Fig. 4a, MS deconvoluted in Fig. S5), the broad heat flow peak around 470 °C is concurrent with the first m/z = 44 MS peak, suggesting two kinetic processes for the first decarbonation reaction (Hinode et al., 1990; D'Assunção et al., 1993). This is largely in agreement with previous thermal decomposition studies on REE hydroxycarbonates (Head and Holley, 1962; Head and Holley, 1963; Hinode et al., 1990; D'Assunção et al., 1993). However, high heating rate (>10 °C/min) was known to make identifications of intermediate carbonate phases difficult (Kim et al., 2018). Thus, other intermediate carbonate phases not represented in reactions (2) and (3) may also be possible during decomposition (Hinode et al., 1990; Sharma et al., 1991). The integration of the deconvoluted m/z = 44 MS curves allows for approximating mole concentration of carbon lost during each deconvoluted step (Table S1), which corresponds well to the theoretical values from reactions (2) and (3). The only exception is the decomposition of NdCO₃OH (Fig. 4e, MS deconvoluted in Fig. S9), which has an additional mass loss event with an onset of 775 °C. That decomposition step corresponds to a mass loss of \sim 6 wt. % and is not accompanied by a CO₂ signal on the MS (or any other signal in the atomic mass range of 1 to 100 amu) or an apparent heat flow peak on the DSC. The additional mass loss step has been previously observed (Shivaramaiah et al., 2016), but its physical origin remains unclear.

Fig. 5 shows the onset temperatures of the decomposition reactions of La_{1-x}Nd_xCO₃OH. The decomposition temperatures of LaCO₃OH and NdCO₃OH agree with those previously determined, which decrease as the atomic

number of REE increases (Wilfong et al., 1964; Charles, 1965; Hinode et al., 1990; De Almeida et al., 2012; Kim et al., 2018). The decomposition temperatures of La_{1-x}Nd_x-CO₃OH solid solutions, however, exhibit a deviation towards higher temperature from that established trend. These average decomposition temperatures were fitted by an inverted second-order polynomial function (Fig. 5). Such enhanced resistance to thermal decomposition may be a result of entropically driven stabilization, with the maximum decomposition temperatures at x = 0.5 reflecting the theoretical configurational entropic maximum for the binary regular solid-solution system. Further support of this phenomenon can be observed from previous TGA-MS studies (Maksimović and Pantó, 1985) (Ar atmosphere and 10 °C/min heating rate) conducted on a rare naturally occurring Nd-hydroxylbastnäsite with the chemical composition of $(Nd_{0.41}La_{0.36}Pr_{0.11}Sm_{0.06}Gd_{0.02}Eu_{0.02}Ca_{0.01})_{\Sigma 0.99}$ $(CO_3)_{1.03}[(OH)_{0.55}F_{0.38}]_{\Sigma 0.93}$ (origins of this mineral will be further described in the Geochemical implications section). This mineral has nearly equimolar concentrations of Nd and La, while containing additional REE within its solid solution, and thus, serves as an excellent naturally occurring analog to our synthetic La_{0.50}Nd_{0.50}CO₃OH sample. By comparing their onset decomposition temperatures (Fig. 4c, Table 2), very good agreements were reached for the onset temperatures of the two steps and the evolved gas content (CO₂ and H₂O). There are also slight increases in thermal stability (\sim 24 and \sim 41 °C for the first and secsteps, respectively) in the natural hydroxylbastnäsite, presumably due to the increased entropic effects from multiple REE mixing and additional F content, the latter of which additionally contributes to the formation of oxyfluorides (Gysi and Williams-Jones, 2015) before the second-stage decomposition that delays further thermal decomposition.

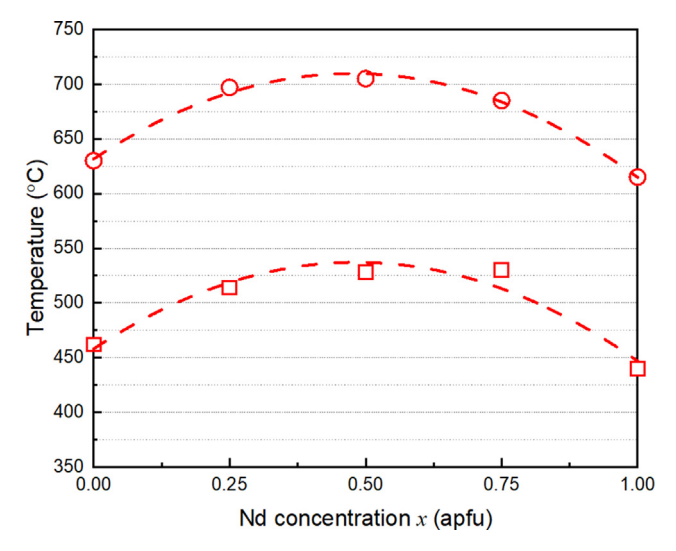


Fig. 5. Onset temperatures of La_{1-x}Nd_xCO₃OH decomposition based on TGA. The onset temperatures of the first decomposition step (reaction (2)) are represented as red squares. The onset temperatures of the second decomposition step (reaction (3)) are represented as light red circles. T1 and T2 curves are the representative onset temperatures for reactions (2) and (3), respectively. The onset of reaction (2) is fit by T1 = $-(338.4 \pm 64.3) \cdot x^2 + (327.1 \pm 67.0) \cdot x + (458.1 \pm 14.1)$ (adjusted $R^2 = 0.8668$). The onset of reaction (3) is fit by T2 = $-(345.1 \pm 21.0) \cdot x^2 + (328.3 \pm 21.9) \cdot x + (631.7 \pm 4.6)$ (adjusted $R^2 = 0.9857$).

The above discoveries emphasize two conclusions for thermal stability of La_{1-x}Nd_xCO₃OH. First, the thermal decomposition temperature of the solid solutions and their endmembers are below 475 °C under ambient pressure, confirming hydroxylbastnäsites to be low-temperature (low-T) mineral phases. Although the decomposition temperature may increase under hydrothermal (elevated P-T) conditions, these results in general support the previous hypothesis on the thermal stability of bastnäsites that OH-phases exist only in low-T environments while F-phases are stable at magmatic conditions (Hsu, 1992; Anenburg et al., 2020). Second, the entropic contribution can stabilize naturally occurring hydroxylbastnäsite solid solutions to relatively high temperatures compared to endmembers by ~ 70 °C near the equimolar of La and Nd where mixing effect is maximized. Noted such entropic effects could be greatly enhanced if more REE cations mix in the matrix (see Boltzmann entropy formula, e.g., Eq. (6)), such as in natural hydroxylbastnäsites where inclusion of several REE (particularly La, Ce, Pr, Nd) are observed (Yang, 2008; Anenburg et al., 2018; Kozlov et al., 2020; Anenburg et al., 2020). The entropically driven thermal stabilization may explain the higher decomposition temperature found in a natural fluoride-bastnäsite-(Ce) sample (Gysi and Williams-Jones, 2015), where the first onset temperature of such Fbastnäsite was reported to be 550 °C, about 100 °C above those of La- and Nd-rich hydroxylbastnäsites. The reported ~ 100 °C enhancement in thermal stability may again be a result of entropic stabilization due to the mixing of Ce, La, Nd, and Pr in fluoride-bastnäsite-(Ce).

4.3. Enthalpic determination, mixing model, and thermodynamic assessment

The enthalpies of formation of $La_{1-x}Nd_xCO_3OH$ from binary oxides and from elements at room temperature

and under the standard condition (Table 3) were derived from experimentally measured $\Delta H_{\rm ds}$. $\Delta H_{\rm f.ox}$ of two endmembers, LaCO₃OH and NdCO₃OH, obtained in this work are $-197.0 \pm 1.9 \text{ kJ/mol}$ and $-165.3 \pm 1.8 \text{ kJ/mol}$, respectively, in excellent agreement with those previously determined (-196.6 \pm 1.6 kJ/mol and -165.0 \pm 3.1 kJ/m ol, respectively) (Shivaramaiah et al., 2016). In addition, there is a negative correlation between $\Delta H_{\rm f.ox}$ of hydroxylbastnäsite and the effective ionic radius of Ln (Fig. 6c), which is also in agreement with previous studies (Shivaramaiah et al., 2016). This implies that REE with larger ionic radii (such as La or Ce) may provide enthalpic stabilization to minor concentrations of other less energetically stable Ln species (e.g., HREE) within the LnCO₃OH phase. The dependence of ΔH_{fox} against Nd concentration can be fitted by the following polynomial

$$\Delta H_{f,ox} = a' + b'x + c'x^2 \tag{4}$$

where $a' = -197.07 \pm 0.10$ kJ/mol, $b' = 44.41 \pm 0.45$ kJ/mol, $c' = -12.67 \pm 0.42$ kJ/mol, with an adjusted $R^2 = 0.9999$. La_{1-x}Nd_xCO₃OH solid solutions all have $\Delta H_{\rm f,ox}$ significantly below zero suggesting their thermodynamic stability compared to their corresponding binary oxides.

On the other hand, despite the demonstrated stability of OH-bastnäsites, their natural presence are still relatively rare compared to the dominating F-rich bastnäsite minerals (Williams-Jones and Wood, 1992; Hsu, 1992). This could be due to the narrower stability fields of OH-bastnäsites than those of F-bastnäsites, suggested by previous calorimetric studies on both OH- and F-bastnäsites (Fig. 7) (Shivaramaiah et al., 2016; Voigt et al., 2016). LaCO₃F has $\Delta H^{\circ}_{\rm f} = -1729.4 \pm 2.7$ kJ/mol (Shivaramaiah et al., 2016), which is more negative than that of LaCO₃OH, $\Delta H^{\circ}_{\rm f} = -1629.3 \pm 2.2$ kJ/mol, measured in this work.

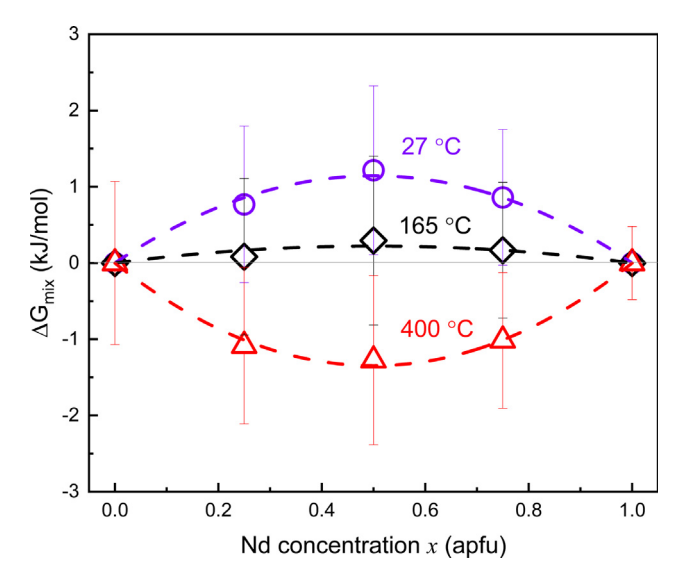


Fig. 6. (a) Enthalpies of drop solution fitted by $\Delta H_{\rm ds} = (150.98 \pm 0.10) - (13.52 \pm 0.44) \cdot x + (12.65 \pm 0.38) \cdot x^2$ (adjusted $R^2 = 0.9984$). (b) Enthalpies of mixing fitted by $\Delta H_{\rm mix} = (12.58 \pm 0.16) \cdot x \cdot (1-x)$ (adjusted $R^2 = 0.9989$). (c) Enthalpy of formation of ${\rm La}_{1-x}{\rm Nd}_x{\rm CO}_3{\rm OH}$ from their corresponding binary oxides at 25 °C, fitted by $\Delta H_{\rm f,ox} = -(197.07 \pm 0.10) + (44.41 \pm 0.45) \cdot x - (12.67 \pm 0.42) \cdot x^2$ (adjusted $R^2 = 0.9999$).

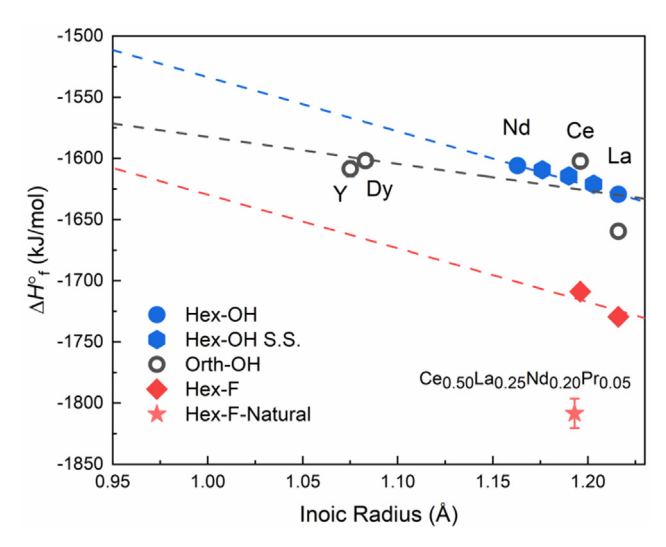


Fig. 7. The standard enthalpy of formation was plotted against the averaged ionic radius of Ln components. ΔH°_{f} of hexagonal LnCO₃OH and hexagonal La_{1-x}Nd_xCO₃OH solid solutions are denoted as *blue* squares and *blue* hexagon, respectively. The *blue dash* line was a linear fitting based on the hexagonal LnCO₃OH data. Orthorhombic LnCO₃OH was denoted as *black* circle, with a *black dashed* linear fitting line describing the enthalpic trend. Two hexagonal LnCO₃F were denoted as *red* rhomboids and a naturally occurring bastnäsite (Ce_{0.5}La_{0.25}-Nd_{0.2}Pr_{0.05}CO₃F) by an *orange* star. Here the *red dashed* line has the same slope of the *blue dashed* line, which was not derived based on the fitting of just the two data, but was shown here as a qualitative comparison of the general enthalpic trend of F-bastnäsites with their and OH-counterparts. Enthalpic values of orthorhombic LnCO₃OH and hexagonal LnCO₃F (Ln = La,Ce) are extracted from (Shivaramaiah et al., 2016), and the enthalpic value of Ce_{0.5}La_{0.25}Nd_{0.2}Pr_{0.05}CO₃F was extracted from (Gysi and Williams-Jones, 2015).

However, the energetic landscape of F-bastnäsites only was only extrapolated from two experimental (La and Ce) results. Additionally, the relative stability of LnCO₃F may also be favored by the entropic effect. This is because that the decomposition of one mole of fluoride-bastnäsite to Ln₂O₃, LnF₃ and CO₂ yields only one mole of CO₂ gas, while that of hydroxylbastnäsite yields two moles of gases (CO₂ and H₂O). Thus, decomposition of hydroxylbastnäsites is more favorable to occur from an entropic perspective, resulting in relatively lower thermodynamic stabilities.

The enthalpies of mixing ($\Delta H_{\rm mix}$) were directly derived from $\Delta H_{\rm ds}$ values (plotted in Fig. 6a) using the thermochemical relations in Table 3. Values of $\Delta H_{\rm mix}$ are plotted in Fig. 6b and fitted by the quadratic polynomial function (with an adjusted $R^2=0.9989$) assuming a regular solution model:

$$\Delta H_{mix} = \Omega \cdot x(1-x) \tag{5}$$

where $\Omega=12.58\pm0.16$ kJ/mol, is the regular solution parameter that quantifies the extent of non-ideality in the mixing of La and Nd in La_{1-x}Nd_xCO₃OH. This small positive value of Ω indicates that the mixing of La and Nd is weakly endothermic, indicating that La_{1-x}Nd_xCO₃OH solid solution is slightly metastable compared to the physical mixture of LaCO₃OH and NdCO₃OH. It also implies a La³⁺ - Nd³⁺ miscibility gap within the hydroxylbastnäsite structural matrix at ambient conditions (Glynn, 2000). This finding may be counterintuitive because all naturally occurring hydroxylbastnäsites are found as solid solutions (Maksimović and Pantó, 1985; Williams-Jones and Wood, 1992; Peishan et al., 1995). The positive $\Delta H_{\rm mix}$ may be attributed to the lattice effects originated from the near-

random distribution of La and Nd in metal sublattices. Previous and current crystallographic studies demonstrated that the hexagonal LnCO₃OH structure (space group P 6) consists of nine coordinated Ln (tricapped trigonal prisms) forming layers of carbonate linked $\frac{2}{\infty}[(OH)Ln_{3/3}]^{2+}$ ions (Michiba et al., 2011; Shivaramaiah et al., 2016). Substituting La (1.216 Å) by the smaller cation Nd (1.163 Å) can cause a slight reduction in the Ln-O bond length, leading to the contraction of the hexagonal unit cell (non-isotropic reduction in both a and c parameters) and a certain degree of lattice strain contributing to the weakly endothermic enthalpy of mixing (Yi et al., 2018). Such a hypothesis may also be appropriate to explain the origin of the high content of La (and Ce with 1.196 Å as the ionic radii of trivalent state) in naturally occurring hydroxylbastnäsites. Since trivalent La and Ce are the softer Ln Lewis acids, they are favored by the large nine coordinated crystallographic sites (Michiba et al., 2011; Kim et al., 2018), and can attenuate the lattice strain induced by the minor presence of heavier Ln to attain phase stability.

Similar results have been reported on REE phosphate systems by calorimetric studies. For instance, in the monazite (LnPO₄, space group $P2_1$ /n) solid solutions, Popa et al. determined the interaction parameters $\Omega=14.0\pm4.1$ kJ/mol, 13.9 ± 8.3 kJ/mol and 23.8 ± 8.7 kJ/mol for La_{1-x}Nd_xPO₄, La_{1-x}Eu_xPO₄, and La_{1-x}Gd_xPO₄, respectively (Popa et al., 2007). Neumeier et al. have determined interaction parameters $\Omega=2.5\pm2.6$ kJ/mol and 11.4 ± 3.1 kJ/mol for La_{1-x}Eu_xPO₄ and La_{1-x}Gd_xPO₄, respectively (Neumeier et al., 2017). Noted that the magnitude of the interaction parameter obtained by Popa et al. for the La_{1-x}Nd_xPO₄ is in good agreement with that of the hexagonal La_{1-x}Nd_xCO₃OH determined in this work. This may be

due to the similar elastic lattice strains in the nine-coordinated environment where metal cations mix, which is commonly shared by monazite and hydroxylbastnäsite in spite of their significant crystallographic differences. When higher REE (smaller ionic radii) are incorporated into the 9-coordinated sites of hydroxylbastnäsite or monazite structures, lattice strain accompanied by an enthalpic penalty is induced on the lattice giving rise to unfavorable enthalpies of mixing (Popa et al., 2007; Migdisov et al., 2019). The interaction parameter of monazite has a positive correlation with the difference between the ionic radii of mixed components (Popa et al., 2007; Mogilevsky, 2007; Neumeier et al., 2017; Migdisov et al., 2019), which could also be translated to the hydroxylbastnäsite systems.

Furthermore, the interaction parameter can be empirically related to the molar volume (V_m) , the difference in the molar volume of the solid solution endmembers $(\Delta V_{\rm m})$, and their corresponding Young's moduli (E) (Brice, 1975; Mogilevsky, 2007; Kowalski and Li, 2016). Currently, there are no experimentally measured elastic moduli of La_{1-x}Nd_xCO₃OH, which, however, may still be estimated through an empirical relation developed for the monazite system: $E \approx 4.8 + 110.6 \cdot r$, where E is the Young's modulus (GPa) and r denotes the ionic radius (Å) of REE (Mogilevsky, 2007). Using this relation, we estimated the Young's modulus of $La_{1-x}Nd_xCO_3OH$ (x = 0.5) to be 136.4 GPa (see details in the SI). Using the estimated E, we further calculated the interaction parameter of La_{1-x}Nd_xCO₃OH based on an empirical relation: $U_e = \frac{E}{6V_e} (\Delta V_m)^2$, where $U_e \approx \Omega$ is the elastic energy (kJ/mol) associated with cation substitution within a lattice and directly to the interaction parameter (SI) (Brice, 1975; Kowalski and Li, 2016). The calculated Ω based on the estimated E, 5.4 kJ/mol, only represents the elastic term that orignates from the volume of mixing, and thus is lower than our calorimetrically determined value ($\Omega = 12.58 \pm 0.16$ kJ/mol). Although the discrepancy may be also due to i) the differences in crystallographic and chemical properties between CO₃OH³⁻ (hydroxylbastnäsite) and PO₄³⁻ (monazite, xenotime), which may result in inaccurate predictions using the above model to the hydroxycarbonate systems, and ii) the lack of experimental data of Young's moduli that can benchmark the empirically derived values.

To further evaluate the thermodynamics of cationic mixing in $\text{La}_{1-x}\text{Nd}_x\text{CO}_3\text{OH}$, the Gibbs free energy of mixing (ΔG_{mix}) was estimated using the regular solution model, where the configurational entropy of mixing $(\Delta S_{\text{mix,config}})$ of La^{3+} and Nd^{3+} in the metal crystallographic sites was calculated using the Boltzmann entropy formula:

$$\Delta S_{mix,config} = -R \cdot [(1-x) \cdot ln(1-x) + x \cdot ln(x)] \tag{6}$$

The vibration entropy of mixing at room temperature $(\Delta S^{\circ}_{\text{mix,vib}})$ can be estimated by using an empirical relation of standard entropy of formation $(S^{\circ}_{298} \, {}^{\circ}_{\text{K}})$ to the molar volume (V_m) of a compound, and is represented by Eq. (7) (Jenkins and Glasser, 2003):

$$S_{298^{\circ}K}^{\circ}/J \cdot K^{-1} mol^{-1} = k \cdot (V_m/^3 \text{ formula unit}^{-1}) + c$$
 (7)

where k and c are the correlation coefficients, 1.262 ± 0.028 /J K⁻¹ mol⁻¹ and 13 ± 5 /J K⁻¹ mol⁻¹, respectively, and formula unit volume V_m is obtained from the experimentally obtained unit cell volume (in Å³) (Table 1) of La_{1-x}Nd_xCO₃OH divided by the z number (18 formula units per unit cell). This value largely reflects the change

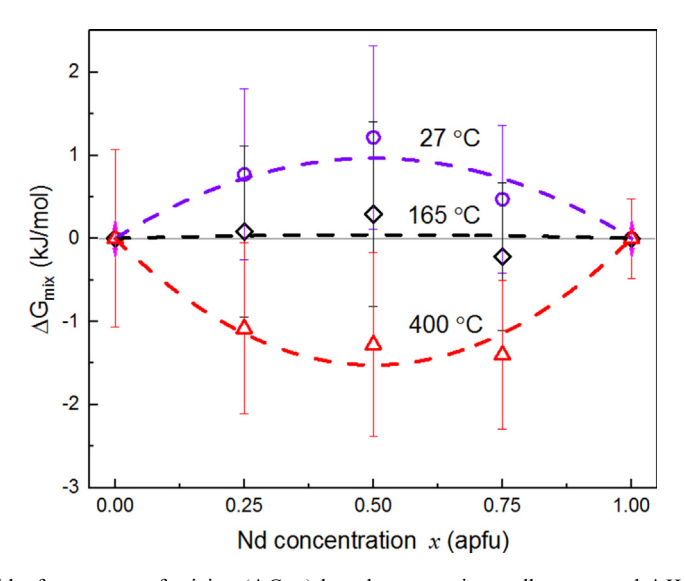


Fig. 8. Estimated trends of Gibbs free energy of mixing ($\Delta G_{\rm mix}$) based on experimentally measured $\Delta H_{\rm mix}$ and calculated $\Delta S_{\rm mix,tot}$ using Eq. (6) and the empirical relation (Eq. (7)) (Jenkins and Glasser, 2003) based on molar volumes (V_m) as obtained from the refinement of XRD results (Table 1). *Purple* circles represent values calculated at ambient temperature (27 °C) and are fitted by $\Delta G_{\rm mix} = (4.57 \pm 0.15) \cdot x \cdot (1-x)$ (adjusted $R^2 = 0.9933$). *Black* rhomboids represent values calculated at synthesis temperature (165 °C) and are fitted by $\Delta G_{\rm mix} = (0.89 \pm 0.15) \cdot x \cdot (1-x)$ (adjusted $R^2 = 0.8615$). *Red* triangles represent values calculated at 400 °C, which is relevant for hydrothermal formation (Hou et al., 2009) and are fitted by $\Delta G_{\rm mix} = -(5.38 \pm 0.14) \cdot x \cdot (1-x)$ (adjusted $R^2 = 0.9960$). All $\Delta G_{\rm mix}$ values were calculated assuming $\Delta H_{\rm mix}$ and $\Delta S_{\rm mix,tot}$ values do not change with temperature.

in the vibrational entropy based on the volumetric change of lattice, and has been successfully applied to estimate S °_{298 °K} for a variety of mineral types (Jenkins and Glasser, 2003). The calculated S°₂₉₈ °_K for La_{1-x}Nd_xCO₃-OH are presented in Table S2. By calculating the difference between S°298 °K of La_{1-x}Nd_xCO₃OH and endmembers (LaCO₃OH and NdCO₃OH), an approximate ΔS°_{mix,vib} can be extracted and combined with the configurational $\Delta S_{\text{mix.config}}$ to yield an appropriate estimate for the total entropy of mixing, $\Delta S_{\text{mix,tot}}$ (Table S2). Here $\Delta S_{\text{mix,config}}$ values are in general a magnitude larger than those of ΔS °_{mix,vib}, suggesting that configurational entropy is the dominant entropic force facilitating mixing in this system. Thus, only $\Delta S_{\text{mix,config}}$ was considered in the following thermodynamic assessment of Gibbs free energy of mixing. The Gibbs free energies of mixing, $\Delta G_{\text{mix}} = \Delta H_{\text{mix}} - \text{T}\Delta S_{\text{mix,tot}}$, at 27 °C, 165 °C, and 400 °C were then obtained and plotted in Fig. 8. These temperatures were chosen to evaluate phase equilibria under ambient, synthetic, and high temperature geothermal conditions (German and Von Damm, 2003). At 27 °C, ΔG_{mix} is positive for all compositions of $La_{1-x}Nd_xCO_3OH$ with a maximum value of 1.26 \pm 1.11 k J/mol at x = 0.5. This suggests that mixing of La and Nd is not spontaneous at ambient temperature, and the formation of exsolution is thermodynamically favorable. When temperature increases to 165 °C, ΔG_{mix} is close to zero for all solid solutions ($\Delta G_{
m mix} = 0.08 \pm 1.03$ kJ/mol, 0.29 \pm 1.11 kJ/mol, and 0.17 \pm 0.89 kJ/mol at x = 0.25, 0.50and 0.75, respectively). Observations during sample synthesis support this thermodynamic assessment indicating that the equimolar La_{0.5}Nd_{0.5}CO₃OH composition was the most challenging phase to synthesize (requiring ~ 14 weeks at 165 °C). However, at temperatures above 250 °C (e.g., \sim 400 °C) where natural bastnäsite ores typically form (Hou et al., 2009), ΔG_{mix} of all compositions are negative, suggesting that La_{1-x}Nd_xCO₃OH solid solutions may form spontaneously from the corresponding hydroxylbastnäsite endmembers in a hypothetical thermodynamic scenario. This implies that stabilization of hexagonal hydroxylbastnäsite solid solutions is driven by entropic effects, in agreement with the onset thermal decomposition temperature trends determined from TGA (Fig. 5). Particularly, La_{0.5}Nd_{0.5}CO₃OH that maximizes configuration entropy (x = 0.5) has the onset of the decomposition of 528 °C, which is higher than the decomposition temperatures of LaCO₃OH and NdCO₃OH endmembers by 66 °C and 88 °C, respectively (Table 2).

4.4. Geochemical implications

The discovery of entropic stabilization of bastnäsite solid solutions at elevated temperatures (>165 °C) has important implications for understanding the mechanisms controlling formation of bastnäsites in natural systems. This is because our calorimetric data suggest a miscibility gap between the La- and Nd-endmembers, while in natural systems, bastnäsites occur exclusively as solid solutions with La, and Nd as typical compositionally dominant components (Gysi and Williams-Jones, 2015; Wang et al., 2020), so entropic contribution must play a major role in stabiliz-

ing the solid solutions at elevated temperatures, which also implies the conditions for natural formation of bastnäsites. Recent modeling work by Liu et al. in 2020 (Liu et al., 2020) has demonstrated that pressure variations have minimal impacts on the paragenesis of LREE minerals (including bastnäsites), with temperature and compositional fluctuations dictating the associated metasomatic processes. Combined with our experimentally determined temperature of hydroxylbastnäsite decomposition (475 ~ 530 °C), this permits to narrow down the temperature interval at which these minerals may be formed in nature. It is therefore tempting to model the formation of hydroxylbastnäsites and to estimate the minimum temperature required for the stabilization of La_{1-x}Nd_xCO₃OH solid solutions under pseudo-natural (La³⁺ and Nd³⁺ are the only REE present) hydrothermal conditions.

To accomplish this, we modelled precipitation of hydroxylbastnäsites triggered by mixing of 10 ml La- and Nd-bearing chloride solution (pH \sim 7) with 1000 ml of carbonate-bearing solution containing NaHCO3, to simulate their formations as a function of temperature under relevant natural conditions. The model of aqueous solution involved H⁺, OH⁻, O₂, H₂, Na⁺, NaOH, NaCl, CO₂, CO₃², HCO₃, Cl⁻, HCl, NaCO₃, NaHCO₃, La³⁺, LaCO₃⁺, LaHCO₃²⁺, LaOH²⁺, LaO⁺, LaOOH, Nd³⁺, NdOH²⁺, Nd(OH)₃, Nd(OH)₂², NdCO₃³, NdHCO₃²⁺, LaCl²⁺, NdCl²⁺, LaCl₂⁺, and NdCl₂⁺. Thermodynamic data were taken from Helgeson et al., 1981; Kestin et al., 1984; Shock and Helgeson, 1988; Oelkers and Helgeson, 1990; Oelkers and Helgeson, 1991; Johnson et al., 1992; Haas et al., 1995; Shock et al., 1997; Sverjensky et al., 1997; Holland and Powell, 1998; Wood et al., 2002; Migdisov et al., 2009. The solid phases accounted for by the model were represented by La- and Nd-enriched hydroxylbastnäsite solid solutions, where the standard enthalpies for pure endmembers and mixing parameters derived in this study were used. It should be noted, that thermodynamic model also requires knowledge of heat capacities (C_p) and standard entropies (S°298 °K, Table S2). However, as a result of the of the experimental data on C_p for these hydroxylbastnäsite phases, we used Neumann-Kopp's rule (Leitner et al., 2013) to estimate the heat capacity functions based on the known C_p of Ln(OH)₃, Ln₂O₃, and CO₂, (Chase, 1998; Diakonov et al., 1998; Konings et al., 2014); the details are discussed in SI. Using the Hch/Unitherm code, (Shvarov and Bastrakov, 1999; Shvarov, 2010) and the regular solution model (Eq. (5)) we performed thermodynamic calculations to evaluate changes in compositions of hydroxylbastnäsite solid solutions as a function of temperature from 25 to 450 °C. The thermodynamic parameters used for modeling solid solutions are summarized in Table S3 in SI. Considering the highly approximate nature of both the entropy and heat capacity used in our calculations, we would like to caveat the outcome of the model presented here as preliminary. There are thus a need for experimental refinements of each of these parameters to develop accurate models of hydroxylbastnäsite formation at elevated temperatures.

The compositional temperature dependence of La_{1-x}Nd_xCO₃OH under equilibrium with aqueous

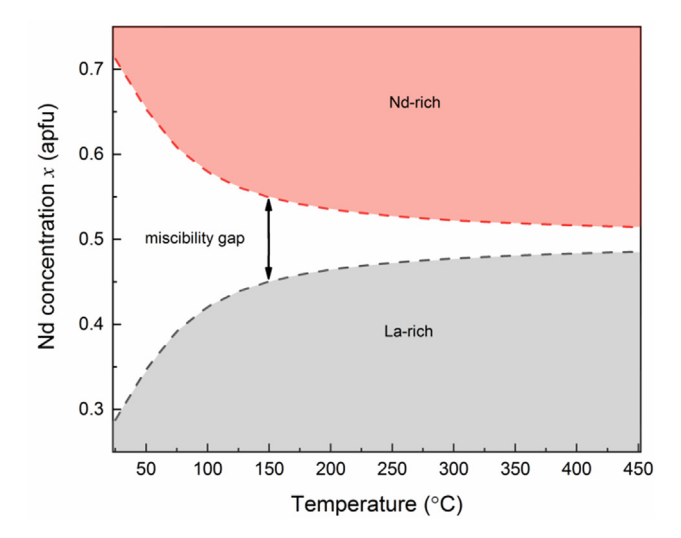


Fig. 9. The concentration of Nd in the Nd- and La-rich hydroxylbastnäsite (initially at 25 °C) as a function of temperature when in equilibrium with NaHCO₃ and LaCl₃/NdCl₃ solutions, where the regular solution model determined from calorimetric work is used. The reversed but same concentration is reported for La in these two hydroxylbastnäsite solid solutions (initially at 25 °C), which is not shown in this figure. The raw data for plotting this **Fig.** can be found in SI (Table S4).

NaHCO₃ and La, Nd-chlorides is demonstrated in Fig. 9 (with detailed results presented in Table S4 in SI). The starting solid phases in equilibrium with the solutions at 25 °C are La- and Nd-rich hydroxylbastnäsites, which have 71.2 mol % La and Nd, respectively. With increasing temperature, there is a significant decrease in the miscibility gap between La and Nd within the La_{1-x}Nd_xCO₃OH matrix. At 450 °C, the stabilization of nearly equimolar solid solutions was found to occur (La and Nd are 51.5 and 48.5 mol %, respectively in the La-rich hydroxylbastnäsite, and vice versa for Nd-rich counterpart). This conclusion further suggests that temperature variance of ΔG_{mix} (discussed above) dictates the formation of the solid solution above 165 °C (Fig. 8). Note the results are based on the mixing model established at 25 °C, which may change at elevated temperatures.

Using these findings, our results can be utilized to gain an approximate understanding of the formational conditions of a given deposit, based on the effects of temperature on the overall favorability of ΔG_{mix} . An example of which is demonstrate by the rare authigenic Nd-dominant hydroxylbastnäsite found in the bauxites deposit near Nikšić, Montenegro (Zagrad deposit) (Maksimović and Pantó, 1985). The deposit is a red karstic bauxite of the Jurassic period (Maksimović and Pantó, 1985). As the mineral is authigenic, it can be used in order to understand the diagenetic conditions of the deposit. The elemental composition of this Nd-hydroxylbastnäsite was determined to be (Nd_{0.41}La_{0.36}- $Pr_{0.11}Sm_{0.06}Gd_{0.02}Eu_{0.02}Ca_{0.01})_{\Sigma 0.99}(CO_3)_{1.03}[(OH)_{0.55}F_{0.38}]$ Σ 0.93 (Maksimović and Pantó, 1985) and thus, serves as an excellent natural analog to the synthetic La_{1-x}Nd_xCO₃OH system examined in this study. Earlier reports suggest that the majority of bastnäsites within the Zagrad deposit were formed by early diagenetic processes (<90 °C) under alkaline, reductive conditions (Radusinović et al., 2017; Radusinović and Papadopoulos, 2021). However, based

on the results of this study, we would suggest the temperatures were significantly higher. Such assertations are based on that the nearly equal molar composition of $\text{La}_{1-x}\text{Nd}_x$ - CO_3OH results are not stabilized until high temperatures are approaching ~ 200 °C (Fig. 8). This would indicate Zagrad deposit had burial depth of ~ 5000 m (Winter, 2013), as there is no other evidence of thermal history in the deposit beside sedimentary diagenesis (Radusinović et al., 2017; Radusinović and Papadopoulos, 2021).

In short, the above thermodynamic investigation suggests a favorable formation of (La, Nd)-bearing hydroxylbastnäsite phases between ~ 150 to 450 °C, which provides additional confirmation to its potential natural occurrence in higher temperatures. Although La_{1-x}Nd_x-CO₃OH solid solutions are only slightly metastable compared to their endmembers at the ambient condition, they can gain entropic stabilization at higher temperatures allowing the initiation of their precipitation out of hydrothermal fluids or their formations through other metasomatic processes (Schoneveld et al., 2015; Anenburg et al., 2018; Anenburg et al., 2020; Wang et al., 2020; Szucs et al., 2021). This explains that although mixing of different REE-binaries in hexagonal hydroxylbastnäsites is not enthalpically favorable, their formation is driven by entropic effects by inclusions of multiple LREEs, in accordance with their corresponding concentrations within the bastnäsite forming REE-bearing fluids (German and Von Damm, 2003; Radusinović and Papadopoulos, 2021).

5. CONCLUSION

In this work, we have studied the thermodynamic properties and phase relations of $La_{1-x}Nd_xCO_3OH$ solid solutions. Thermal decomposition pathways of $La_{1-x}Nd_xCO_3OH$ were determined by TGA-DSC-MS, with the solid solutions exhibiting increased thermal stability

compared to their endmembers, while also confirming these hydroxylbastnäsites being low-T mineral phases. High temperature oxide melt drop solution calorimetry was used to determine $\Delta H_{f,ox}$, $\Delta H_{f,ox}$, and ΔH_{mix} of La_{1-x}Nd_xCO₃OH solid solutions at room temperature, which indicate the enthalpic metastability of La_{1-x}Nd_xCO₃OH solid solutions with respect to LaCO₃OH and NdCO₃OH. Detailed analysis reveals a regular solution model for the mixing of La and Nd. Furthermore, the unit cell parameters follow nearly linear relations as a function of Nd content, suggesting a random distribution of La and Nd in the metal sites, enabling the estimation of ΔS_{mix} by the Boltzmann entropy formula. Combining entropy and enthalpy leads to the evaluation of $\Delta G_{\rm mix}$ at 27, 165, and 400 °C, which reveals that the formation of La_{1-x}Nd_xCO₃OH solid solutions may become favorable at temperatures encountered at hydrothermal or latestage diagenetic conditions. These results suggest that entropy plays an important role in the stabilization of naturally occurring multi-cationic hexagonal hydroxylbastnäsite solid solutions. Further thermodynamic calculations confirm and narrow down the temperature range (~150 to 450 °C), within which the formation of (La, Nd)-bearing hydroxylbastnäsites become favorable.

DECLARATION OF COMPETING INTEREST

The authors declare that they have no known competing financial interests or personal relationships that could have appeared to influence the work reported in this paper.

ACKNOWLEDGMENTS

We acknowledge the support by the institutional funds from the Department of Chemistry and New Faculty Seed Grant from ORAP at Washington State University in the early stage, and later supported by the National Science Foundation (NSF), Division of Earth Sciences, under award No. 2149848. Support of V.G.G. and A. S. is partially through the U.S. Department of Energy. Office of Nuclear Energy, grant DE-NE0008582. Research presented in this article was also supported by the Laboratory Directed Research and Development (LDRD) program of Los Alamos National Laboratory (LANL): project 20190057DR and Center for Space and Earth Science (CSES). CSES is funded by LANL's Laboratory Directed Research and Development (LDRD) program under project number 20180475DR. LANL, an affirmative action/equal opportunity employer, is managed by Triad National Security, LLC, for the National Nuclear Security Administration of the U.S. Department of Energy under contract 89233218CNA000001. Portions of this research were also supported by collaboration, services, and infrastructure through the Nuclear Science Center User Facility at WSU, the WSU-PNNL Nuclear Science and Technology Institute, and Alexandra Navrotsky Institute for Experimental Thermodynamics. This research used resources of the Advanced Photon Source, a U.S. Department of Energy (DOE) Office of Science User Facility operated for the DOE Office of Science by Argonne National Laboratory under Contract No. DE-AC02-06CH11357.

RESEARCH DATA

Research Data associated with this article can be accessed at http://doi.org/10.17632/xmpp8pz8g9.1.

APPENDIX A. SUPPLEMENTARY MATERIAL

Supplementary material to this article can be found online at https://doi.org/10.1016/j.gca.2022.04.002.

REFERENCES

- Aakeröy C. B., Seddon K. R. and Leslie M. (1992) Hydrogenbonding contributions to the lattice energy of salts for second harmonic generation. Struct. Chem. 3, 63-65.
- Adachi G.-Y. and Imanaka N. (1998) The binary rare earth oxides. *Chem. Rev.* 4, 1479–1514.
- De Almeida L., Grandjean S., Vigier N. and Patisson F. (2012) New insights on the thermal decomposition of lanthanide(III) and actinide(III) oxalates: from neodymium and cerium to plutonium. *Eur. J. Inorg. Chem.* **31**, 4986–4999.
- Anenburg M., Burnham A. D. and Mavrogenes J. (2018) REE redistribution textures in altered fluorapatite: symplectites, veins, and phosphate-silicate-carbonate assemblages from the Nolans Bore P-REE-Th deposit, Northern Territory, Australia. Can. Mineral. 56, 331–354.
- Anenburg M., Mavrogenes J. A., Frigo C. and Wall F. (2020) Rare earth element mobility in and around carbonatites controlled by sodium, potassium, and silica. *Sci. Adv.* **6**, 6570.
- Anon (2020) National Minerals Information Center: Rare Earths Statistics and Information. U.S.G.S..
- Brice J. (1975) Some thermodynamic aspects of the growth of strained crystals. *J. Cryst. Growth* **28**, 249–253.

Bruker Nano GmbH (2010a) S2 picofoxTM.

Bruker Nano GmbH (2010b) Spectra 7.

- Cantrell K. J. and Byrne R. H. (1987) Rare earth element complexation by carbonate and oxalate ions. *Geochim. Cos*mochim. Acta 51, 597–605.
- Carroll S. A. (1993) Precipitation of Nd-Ca carbonate solid solution at 25 °C. Geochim. Cosmochim. Acta 57, 3383–3393.
- Castor S. B. (2008) Rare earth deposits of North America. *Resour. Geol.* **58**, 337–347.
- Chai L. and Navrotsky A. (1996) Synthesis, characterization, and enthalpy of mixing of the (Fe, Mg)CO₃ solid solution. *Geochim. Cosmochim. Acta* **60**, 4377–4383.
- Charles R. G. (1965) Rare-earth carbonates prepared by homogeneous precipitation. J. Inorg. Nucl. Chem. 27, 1489–1493.
- Chase M. W. J. (1998) NIST-JANAF thermochemical tables, fourth edition. J. Phys. Chem. Ref. Data Monogram 9, 1–1951.
- Cheng J., Navrotsky A., Zhou X. D. and Anderson H. U. (2005) Enthalpies of formation of LaMO₃ perovskites (M = Cr, Fe Co, and Ni). *J. Mater. Res.* **20**, 191–200.
- Chizmeshya A., Bauer M. and Kouvetakis J. (2003) Experimental and theoretical study of deviations from Vegard's Law in the Sn_xGe_{1-x} system. *Chem. Mater.* **15**, 2511–2519.
- Cho W. J., Kim J. S. and Choi H. J. (2014) Hydrothermal modeling for the efficient design of thermal loading in a nuclear waste repository. *Nucl. Eng. Des.* 276, 241–248.
- Christensen A. (1973) Hydrothermal preparation of rare earth hydroxycarbonates. The crystal structure of NdOHCO₃. *Acta Chem. Scand.* **27**, 2973–2982.

- Chung C. K., Guo X., Wang G., Wilson T. L., White J. T., Nelson A. T., Shelyug A., Boukhalfa H., Yang P., Batista E. R., Migdisov A. A., Roback R. C., Navrotsky A. and Xu H. (2019) Enthalpies of formation and phase stability relations of USi, U₃Si₅ and U₃Si₂. J. Nucl. Mater. 523, 101–110.
- Clavier N., Podor R. and Dacheux N. (2011) Crystal chemistry of the monazite structure. *J. Eur. Ceram. Soc.* **31**, 941–976.
- Collongues R. (1992) Nonstoichiometry in oxides. *Prog. Cryst. Growth Charact. Mater.* **25**, 203–240.
- D'Assunção L. M., Ionashiro M., Rasera D. E. and Giolito I. (1993) Thermal decomposition of the hydrated basic carbonates of lanthanides and yttrium in CO₂ atmosphere. *Thermochim. Acta* 219, 225–233.
- Diakonov I. I., Ragnarsdottir K. V. and Tegirov B. R. (1998) Standard thermodynamic properties and heat capacity equations of rare earth hydroxides II: Ce(III)-, Pr-, Sm-, Eu(III)-, Gd-, Tb-, Dy-, Ho-, Er-, Tm-, Yb-, and Y-hydroxides. Comparison of thermochemical and solubility data. *Chem. Geol.* 151, 327–347.
- Du Fou de Kerdaniel E., Clavier N., Dacheux N., Terra O. and Podor R. (2007) Actinide solubility-controlling phases during the dissolution of phosphate ceramics. *J. Nucl. Mater.* **362**, 451–458.
- Essington M. E. and Mattigod S. V. (1985) Lanthanide solid phase speciation. Soil Sci. Soc. Am. J. 49, 1387–1393.
- Ewing R. C., Whittleston R. A. and Yardley B. W. D. (2016) Geological disposal of nuclear waste: A primer. *Elements* 12, 233–237.
- Fan H. R., Yang K. F., Hu F. F., Liu S. and Wang K. Y. (2016) The giant Bayan Obo REE-Nb-Fe deposit, China: Controversy and ore genesis. *Geosci. Front.* 7, 335–344.
- Farrow C. L., Juhas P., Liu J. W., Bryndin D., Božin E. S., Bloch J., Proffen T. and Billinge S. J. L. (2007) PDFfit2 and PDFgui: computer programs for studying nanostructure in crystals. *J. Phys. Condens. Matter* 19, 335219.
- Fitzgibbon G. C., Pavone D. and Holley C. E. (1968) Enthalpy of Formation of Nd₂O₃-Hexagonal. *J. Chem. Eng. Data* **13**, 547–548.
- German C. R. and Von Damm K. L. (2003) Hydrothermal processes. In *Treatise, on geochemistry, Vol. 6. The oceans and marine geochemistry* (eds. H. D. Holland, K. K. Turekian and H. Elderfield). Elsevier-Pergamon, Oxford, UK, pp. 181–222.
- Glynn P. (2000) Solid-solution solubilities and thermodynamics: Sulfates, carbonates and halides. Rev. Mineral. Geochem. 40, 481–511
- Goodenough K. M., Schilling J., Jonsson E., Kalvig P., Charles N., Tuduri J., Deady E. A., Sadeghi M., Schiellerup H., Müller A., Bertrand G., Arvanitidis N., Eliopoulos D. G., Shaw R. A., Thrane K. and Keulen N. (2016) Europe's rare earth element resource potential: An overview of REE metallogenetic provinces and their geodynamic setting. *Ore Geol. Rev.* 72, 838–856.
- Gramaccioli C. M., Diella V. and Demartin F. (1999) The role of fluoride complexes in REE geochemistry and the importance of 4f electrons: some examples in minerals. *Eur. J. Mineral.* 11, 983–992.
- Gschneider K. A., Bunzli J. and Pecharsky V. (2011) Handbook on the physics and chemistry of rare earths: optical spectroscopy. Vol 37., North-Holland.
- Gschneidner K. A. (2011) The rare earth crisis-the supply/demand situation for 2010–2015. *Mater. Matters* 6.
- Guo X., Boukhalfa H., Mitchell J. N., Ramos M., Gaunt A. J., Migliori A., Roback R. C., Navrotsky A. and Xu H. (2019a) Sample seal-and-drop device and methodology for high temperature oxide melt solution calorimetric measurements of PuO₂. Rev. Sci. Instrum. 90, 044101.

- Guo X., Kukkadapu R. K., Lanzirotti A., Newville M., Engelhard M. H., Sutton S. R. and Navrotsky A. (2015) Charge-coupled substituted garnets $(Y_{3-x}Ca_{0.5x}M_{0.5x})Fe_5O_{12}$ (M=Ce,Th): Structure and stability as crystalline nuclear waste forms. *Inorg. Chem.* **54**, 4156–4166.
- Guo X., Lü X., White J. T., Benmore C. J., Nelson A. T., Roback R. C. and Xu H. (2019b) Bulk moduli and high pressure crystal structure of U₃Si₂, *J. Nucl. Mater.* **523**, 135–142.
- Guo X., Szenknect P., Mesbah A., Clavier N., Poinssot C., Wu D., Xu H., Dacheux N., Ewing R. C. and Navrotsky A. (2016) Energetics of a Uranothorite (Th_{1-x}U_xSiO₄) solid solution. *Chem. Mater.* 28, 7117–7124.
- Guo X., Tavakoli A. H., Sutton S., Kukkadapu R. K., Qi L., Lanzirotti A., Newville M., Asta M. and Navrotsky A. (2014a) Cerium substitution in yttrium iron garnet: Valence state, structure, and energetics. *Chem. Mater.* 26, 1133–1143.
- Guo X., Ushakov S. V., Labs S., Curtius H., Bosbach D. and Navrotsky A. (2014b) Energetics of metastudtite and implications for nuclear waste alteration. *Proc. Natl. Acad. Sci. U. S.* A. 111, 17737–17742.
- Guo X., White J. T., Nelson A. T., Migdisov A., Roback R. and Xu H. (2018) Enthalpy of formation of U₃Si₂: A hightemperature drop calorimetry study. J. Nucl. Mater. 507, 44–49.
- Guo X. and Xu H. (2017) Enthalpies of formation of polyhalite: A mineral relevant to salt repository. J. Chem. Thermodyn. 114, 44–47.
- Gysi A. P. and Williams-Jones A. E. (2015) The thermodynamic properties of bastnäsite-(Ce) and parisite-(Ce). *Chem. Geol.* 392, 87–101.
- Haas J. R., Shock E. L. and Sassani D. C. (1995) Rare earth elements in hydrothermal systems: Estimates of standard partial molal thermodynamic properties of aqueous complexes of the rare earth elements at high pressures and temperatures. *Geochim. Cosmochim. Acta* **59**, 4329–4350.
- Head E. L. and Holley C. E. (1962) The preparation and thermal decomposition of some rare earth carbonates. *Atomic Energy Commission*.
- Head E. L. and Holley C. E. (1963) The preparation and thermal decomposition of the carbonates of Tb, Dy, Ho, Er, Tm, Yb, Lu, Y, and Sc. *Atomic Energy Commission*.
- Hedrick C. S. B. (2006) Rare earth elements. In *Industrial Minerals Volume*, 7th Edition, Society for Mining, metallurgy, and Exploration, Littleton, Colorado, pp. 769–792.
- Helgeson H. C., Kirkham D. H. and Flowers G. C. (1981) Theoretical prediction of the thermodynamic behavior of aqueous electrolytes at high pressures and temperatures: IV. Calculation of activity coefficients, osmotic coefficients, and apparent molal and standard and relative partial molal properties to 600°. *Am. J. Sci.* **281**, 1249–1516.
- Heuser J. M., Palomares R. I., Bauer J. D., Rodriguez M. J. L., Cooper J., Lang M., Scheinost A. C., Schlenz H., Winkler B., Bosbach D., Neumeier S. and Deissmann G. (2018) Structural characterization of (Sm, Tb)PO₄ solid solutions and pressure-induced phase transitions. J. Eur. Ceram. Soc. 38, 4070–4081.
- Hinode H., Sharma R. and Eyring L. (1990) A study of the decomposition of neodymium hydroxy carbonate and neodymium carbonate hydrate. J. Solid State Chem. 84, 102–117.
- Holland T. J. and Powell R. (1998) An internally consistent thermodynamic data set for phases of petrological interest. *J. Metamorph. Geol.* **16**, 309–343.
- Hou Z., Tian S., Xie Y., Yang Z., Yuan Z., Yin S., Yi L., Fei H., Zou T., Bai G. and Li X. (2009) The Himalayan Mianning-Dechang REE belt associated with carbonatite-alkaline complexes, eastern Indo-Asian collision zone, SW China. *Ore Geol. Rev.* 36, 65–89.

- Hsu L. C. (1992) Synthesis and stability of bastnaesites in a part of the system (Ce, La)-F-H-C-O. *Mineral. Petrol.* 47, 87–101.
- Jenkins H. D. B. and Glasser L. (2003) Standard absolute entropy, S^o₂₉₈, values from volume or density. 1. Inorganic Materials. *Inorg. Chem.* 42, 8702–8708.
- Johnson J. W., Oelkers E. H. and Helgeson H. C. (1992) SUPCRT92: A software package for calculating the standard molal thermodynamic properties of minerals, gases, aqueous species, and reactions from 1 to 5000 bar and 0 to 1000°C. Comput. Geosci. 18, 899–947.
- Kagan H. B. (2002) Introduction: Frontiers in lanthanide chemistry. Chem. Rev. 102, 1805–1806.
- Kalintsev A., Migdissov A., Alcorn C., Baker J., Brugger J., Mayanovic R. A., Akram N., Guo X., Xu H., Boukhalfa H., Caporuscio F. A., Viswanathan H., Jove-Colon C., Wang Y., Matteo E. and Roback R. (2021) Uranium carbonate complexes demonstrate drastic decrease in stability at elevated temperatures. *Commun. Chem.* 4, 1–8.
- Kanazawa Y. and Kamitani M. (2006) Rare earth minerals and resources in the world. *J. Alloys Compd.* **408–412**, 1339–1343.
- Karraker D. G. (1970) Coordination of trivalent lanthanide ions. *J. Chem. Eduction* **47**, 424–430.
- Kestin J., Sengers J. V., Kamgar-Parsi B. and Sengers J. M. H. L. (1984) Thermophysical properties of fluid H₂O. J. Phys. Chem. Ref. Data 13, 175–183.
- Kim P., Anderko A., Navrotsky A. and Riman R. (2018) Trends in structure and thermodynamic properties of normal rare earth carbonates and rare earth hydroxycarbonates. *Minerals* 8, 106.
- Konings R., Benes O., Kovacs A., Manara D., Sedmidubsky G. L.,
 Iorish V., Yungman V., Shenyavskaya E. and Osina E. (2014)
 The thermodynamic properties of the f-elements and their compounds. Part 2. The Lanthanide and Actinide Oxides. *J. Phys. Chem. Ref. Data* 43, 9–11.
- Kowalski P. M. and Li Y. (2016) Relationship between the thermodynamic excess properties of mixing and the elastic moduli in the monazite-type ceramics. *J. Eur. Ceram. Soc.* 36, 2093–2096.
- Kozlov E., Fomina E., Sidorov M., Shilovskikh V., Bocharov V., Chernyavsky A. and Huber M. (2020) The Petyayan-Vara Carbonatite-Hosted Rare Earth Deposit (Vuoriyarvi, NW Russia): Mineralogy and geochemistry. *Miner.* 10, 73.
- Kutlu I. and Meyer G. (1999) Basische Carbonate des Dysprosiums: Dy₂O₂(CO₃) und Dy(OH)(CO₃). Z. Anorg. Allg. Chem. 625, 402–406.
- Leitner J., Sedmidubský D., Ružička K. and Svoboda P. (2013) Calorimetric determination of heat capacity, entropy and enthalpy of mixed oxides in the system CaO-SrO-Bi₂O₃-Nb₂O₅-Ta₂O₅. Appl. Calorim. A Wide Context - Differ. Scanning Calorimetry, Isothermal Titration Calorim. Microcalorim., 385-406.
- Lide D. (2004) Abundance of elements in the Earth's crust and in the sea, in sec. 14 of CRC handbook of physics and chemistry—A ready-reference book of chemical and physical data, 85th ed.,. CRC Press, Boca Raton, Fla.
- Liu S., Ding L. and Fan H. R. (2020) Thermodynamic constraints on REE mineral paragenesis in the Bayan Obo REE-Nb-Fe Deposit, China. *Miner.* 10, 495.
- Long K. R., Van Gosen B. S., Foley N. K. and Cordier D. (2010)

 The Principal Rare Earth Elements Deposits of the United

 States—A Summary of Domestic Deposits and a Global

 Perspective. U.S.G.S..
- Long K. R., Van Gosen B. S., Foley N. K. and Cordier D. (2012)
 The principal rare earth elements deposits of the United States:
 A summary of domestic deposits and a global perspective. In Non-Renewable Resource Issues: Geoscientific and Societal Challenges. Springer, Netherlands, pp. 131–155.

- Maksimović Z. and Pantó G. (1985) Hydroxyl-bastnaesite-(Nd), a new mineral from Montenegro, Yugoslavia. *Mineral. Mag.* 49, 717–720.
- Marcial J., Zhang Y., Zhao X., Xu H., Mesbah A., Nienhuis E. T., Szenknect S., Neuefeind J. C., Lin J., Qi L., Migdisov A. A., Ewing R. C., Dacheux N., McCloy J. S. and Guo X. (2021) Thermodynamic non-ideality and disorder heterogeneity in actinide silicate solid solutions. npj Mater Degrad 5, 1–14.
- McLellan B., Corder G. and Ali S. (2013) Sustainability of rare earths—An overview of the state of knowledge. *Minerals* 3, 304–317.
- Meinrath G. and Takeishi H. (1993) Solid-liquid equilibria of Nd³⁺ in carbonate solutions. J. Alloys Compd. 194, 93–99.
- Michiba K., Tahara T., Nakai I., Miyawaki R. and Matsubara S. (2011) Crystal structure of hexagonal RE(CO₃)OH. Zeitschrift fur Krist. 226, 518–530.
- Migdisov A. A., Williams-Jones A. E. and Wagner T. (2009) An experimental study of the solubility and speciation of the Rare Earth Elements (III) in fluoride- and chloride-bearing aqueous solutions at temperatures up to 300 °C. *Geochim. Cosmochim. Acta* **73**, 7087–7109.
- Migdisov A. A., Guo X., Nisbet H., Xu H. and Williams-Jones A. E. (2019) Fractionation of REE, U, and Th in natural oreforming hydrothermal systems: Thermodynamic modeling. *J. Chem. Thermodyn.* 128, 305–319.
- Mogilevsky P. (2007) On the miscibility gap in monazite–xenotime systems. *Phys. Chem. Miner.* **34**(3), 201–214.
- Navrotsky A. (2014) Progress and new directions in calorimetry: A 2014 perspective. J. Am. Ceram. Soc. 97, 3349–3359.
- Navrotsky A., Rapp R. P., Smelik E., Pamela B., Circone S., Chai L. and Bose K. (1994) The behavior of H₂O and CO₂ in hightemperature lead borate solution calorimetry of volatile-bearing phases. Am. Mineral. 79, 1099–1109.
- Neumeier S., Kegler P., Arinicheva Y., Shelyug A., Kowalski P. M., Schreinemachers C., Navrotsky A. and Bosbach D. (2017) Thermochemistry of La_{1-x}Ln_xPO₄-monazites (Ln = Gd, Eu). *J. Chem. Thermodyn.* **105**, 396–403.
- Nisbet H., Migdisov A. A., Williams-Jones A. E., van Hinsberg V. J., Xu H. and Roback R. (2022) The solubility of thorium in carbonate-bearing solutions at hydrothermal conditions. *Geochim. Cosmochim. Acta.* 330, 80–92.
- Oelkers E. H. and Helgeson H. C. (1991) Calculation of activity coefficients and degrees of formation of neutral ion pairs in supercritical electrolyte solutions. *Geochim. Cosmochim. Acta* 55, 1235–1251.
- Oelkers E. H. and Helgeson H. C. (1990) Triple-ion anions and polynuclear complexing in supercritical electrolyte solutions. *Geochim. Cosmochim. Acta* **54**, 727–738.
- Olds T. A., Karcher S. E., Kriegsman K. W., Guo X. and McCloy J. S. (2020) Oxidation and anion lattice defect signatures of hypostoichiometric lanthanide-doped UO₂. J. Nucl. Mater. 530, 151959.
- Pathak A. K., Khan M., Gschneidner K. A., McCallum R. W., Zhou L., Sun K., Dennis K. W., Zhou C., Pinkerton F. E., Kramer M. J. and Pecharsky V. K. (2015) Cerium: An unlikely replacement of dysprosium in high performance Nd-Fe-B permanent magnets. Adv. Mater. 27, 2663–2667.
- Peishan Z., Xueming Y. and Kejie T. (1995) *Mineralogy and Geology of Rare Earths in China*. Science Press, Beijing.
- Peters J. A., Djanashvili K., Geraldes C. F. G. C. and Platas-Iglesias C. (2020) The chemical consequences of the gradual decrease of the ionic radius along the Ln-series. *Coord. Chem. Rev.* 406, 213146.
- Polinski M. J., Grant D. J., Wang S., Alekseev E. V., Cross J. N., Villa E. M., Depmeier W., Gagliardi L. and Albrecht-Schmitt T. E. (2012) Differentiating between trivalent lanthanides and actinides. J. Am. Chem. Soc. 134, 10682–10692.

- Popa K., Konings R. J. M. and Geisler T. (2007) High-temperature calorimetry of (La_{1-x}Ln_x)PO₄ solid solutions. *J. Chem. Ther-modyn.* 39, 236–239.
- Qi J., Guo X., Mielewczyk-Gryn A. and Navrotsky A. (2015) Formation enthalpies of LaLnO₃ (Ln = Ho, Er, Tm and Yb) interlanthanide perovskites. J. Solid State Chem. 227, 150–154.
- Radusinović S., Jelenković R., Pačevski A., Simić V., Boţović D., Holclajtner-Antunović I. and Zivotić D. (2017) Content and mode of occurrences of rare earth elements in the Zagrad karstic bauxite deposit (Nikšić area, Montenegro). Ore Geol. Rev. 80, 406–428.
- Radusinović S. and Papadopoulos A. (2021) The potential for REE and associated critical metals in Karstic Bauxites and Bauxite Residue of Montenegro. *Miner.* 11, 975.
- Ravel B. and Newville M. (2005) ATHENA, ARTEMIS, HEPHAESTUS: Data analysis for X-ray absorption spectroscopy using IFEFFIT. J. Synchrotron Radiat. 12, 537–541.
- Ringwood A. E., Kesson S. E., Ware N. G., Hibberson W. and Major A. (1979) Immobilisation of high level nuclear reactor wastes in SYNROC. *Nature* 278, 219–223.
- Rorif F., Fuger J. and Desreux J. (2005) Thermochemistry of selected trivalent lanthanide and americium compounds: orthorhombic and hexagonal hydroxycarbonates. *Radiochim.* Acta 93, 103–110.
- Rudnick R. L. and Gao S. (2003) Composition of the continental crust. In *Treatise on Geochemistry*. Elsevier Inc., pp. 1–64.
- Runde W., Meinrath G. and Kim J. I. (1992) A study of solid-liquid phase equilibria of trivalent lanthanide and actinide ions in carbonate systems. *Radiochim. Acta* 58–59, 93–100.
- Santos-Martins D. and Forli S. (2020) Charting hydrogen bond anisotropy. J. Chem. Theory Comput. 16, 2846–2856.
- Schlenz H., Dellen J., Kegler P., Gatzen C., Schreinemachers C., Shelyug A., Klinkenberg M., Navrotsky A. and Bosbach D. (2019) Structural and thermodynamic mixing properties of La_{1-x}Nd_xPO₄ monazite-type solid solutions. *J. Solid State Chem.* 270, 470–478.
- Schmitt A., Lorenz H., Richter H. and Kunze G. (1991) Discontinuous process for the precipitation of rare earth carbonates from aqueous solutions containing other anions and cations. *DE patent*, *DD292216*.
- Schoneveld L., Spandler C. and Hussey K. (2015) Genesis of the central zone of the Nolans Bore rare earth element deposit, Northern Territory, Australia. *Contrib. to Mineral. Petrol.* 170 (2), 1–22.
- Schulz K. J., DeYoung J. H., Seal R. R. and Bradley D. C. (2019)

 Critical Mineral Resources of the United States: Economic and

 Environmental Geology and Prospects for Future Supply. U.S.G.
 S.
- Schweda E. and Kang Z. (2005) Structural features of rare earth oxides. In *Binary Rare Earth Oxides*. Springer, Netherlands, pp. 57–93.
- Sharma R., Hinode H. and Eyring L. (1991) A study of the decomposition of praseodymium hydroxy carbonate and praseodymium carbonate hydrate. *J. Solid State Chem.* 92, 401–419.
- Shivaramaiah R., Anderko A., Riman R. E. and Navrotsky A. (2016) Thermodynamics of bastnaesite: A major rare earth ore mineral. Am. Mineral. 101, 1129–1134.
- Shock E. L. and Helgeson H. C. (1988) Calculation of the thermodynamic and transport properties of aqueous species at high pressures and temperatures: Correlation algorithms for ionic species and equation of state predictions to 5 kb and 1000 °C. *Geochim. Cosmochim. Acta* **52**, 2009–2036.
- Shock E. L., Sassani D. C., Willis M. and Sverjensky D. A. (1997) Inorganic species in geologic fluids: Correlations among stan-

- dard molal thermodynamic properties of aqueous ions and hydroxide complexes. *Geochim. Cosmochim. Acta* **61**, 907–950.
- Shvarov Y. V. (2010) OptimA: A program for the calculation of the free energies of dissolved aqueous species from the results of chemical experiments. (http://www.geol.msu.ru/deps/geochems/soft/).
- Shvarov Y. V. and Bastrakov E. (1999) HCh: a software package for geochemical equilibrium modelling. *User's Guide, Australian Geological Survey Organization Record* **25**, 60.
- Smith M. P., Henderson P. and Campbell L. S. (2000) Fractionation of the REE during hydrothermal processes: Constraints from the Bayan Obo Fe-REE-Nb deposit, Inner Mongolia, China. *Geochim. Cosmochim. Acta* 64, 3141–3160.
- Strzelecki A. C., Barral T., Estevenon P., Mesbah A., Goncharov V., Baker J., Bai J., Clavier N., Szenknect S., Migdissov A., Xu H., Ewing R. C., Dacheux N. and Guo X. (2021) The role of water and hydroxyl groups in the structures of stetindite and coffinite, MSiO₄ (M = Ce, U). *Inorg. Chem.* 60, 718–735.
- Strzelecki A. C., Bourgeois C., Kriegsman K. W., Estevenon P., Wei N., Szenknect S., Mesbah A., Wu D., Ewing R. C., Dacheux N. and Guo X. (2020a) Thermodynamics of CeSiO₄: Implications for actinide orthosilicates. *Inorg. Chem.* 59, 13174–13183.
- Strzelecki A. C., Kriegsman K., Estevenon P., Goncharov V., Bai J., Szenknect S., Mesbah A., Wu D., McCloy J. S., Dacheux N. and Guo X. (2020b) High temperature thermodynamics of cerium silicates, A-Ce₂Si₂O₇ and Ce_{4.67}(SiO₄)₃O. *ACS Earth Sp. Chem.* **4**, 2129–2143.
- Sverjensky D. A., Shock E. L. and Helgeson H. C. (1997) Prediction of the thermodynamic properties of aqueous metal complexes to 1000°C and 5 kb. *Geochim. Cosmochim. Acta* 61, 1359–1412.
- Szucs A. M., Stavropoulou A., O'Donnell C., Davis S. and Rodriguez - Blanco J. D. (2021) Reaction pathways toward the formation of Bastnäsite: Replacement of calcite by rare earth carbonates. Cryst. Growth Des. 21, 512–527.
- Tang Z., Huang Z., Han W., Qi J., Shi Y., Ma N., Zhang Y., Guo X. and Lu T. (2020) Uranium-incorporated pyrochlore La₂(-U_xMg_xZr_{1-2x)2}O₇ nuclear waste form: Structure and phase stability. *Inorg. Chem.* 59, 9919–9926.
- Thompson P., Cox D. E. and Hastings J. B. (1987) Rietveld refinement of Debye-Scherrer synchrotron X-ray data from Al₂O₃, *J. Appl. Crystallogr.* **20**, 79–83.
- Toby B. H., Madden T. J., Suchomel M. R., Baldwin J. D. and Von Dreele R. B. (2013) A scanning CCD detector for powder diffraction measurements. J. Appl. Crystallogr. 46, 1058–1063.
- Le Tonquesse S., Pasturel M., Demange V., Tayal A., Solari P. L. and Prestipino C. (2019) X-ray absorption study on the origin of the deviation from Vegard's law for U(Al_{1-x}Ge_x)₃ solid solution. *J. Nucl. Mater.* **526**, 151772.
- Ushakov S. V., Helean K. B., Navrotsky A. and Boatner L. A. (2001) Thermochemistry of rare-earth orthophosphates. *J. Mater. Res.* **16**, 2623–2633.
- Vallina B., Rodriguez-Blanco J. D., Blanco J. A. and Benning L. G. (2014) The effect of heating on the morphology of crystalline neodymium hydroxycarbonate, NdCO₃OH. *Mineral. Mag.* **78**, 1391–1397.
- Vallina B., Rodriguez-Blanco J. D., Brown A. P., Blanco J. A. and Benning L. G. (2015) The role of amorphous precursors in the crystallization of La and Nd carbonates. *Nanoscale* 7, 12166– 12179
- Vegard L. (1921) Die Konstitution der Mischkristalle und die Raumfüllung der Atome. Zeitschrift für Phys. 5, 17–26.
- Voigt M., Rodriguez-Blanco J. D., Vallina B., Benning L. G. and Oelkers E. H. (2016) An experimental study of hydroxylbast-

- nasite solubility in aqueous solutions at 25 °C. *Chem. Geol.* **430**, 70–77.
- Voskanyan A. A., Goncharov V. G., Novendra N., Guo X. and Navrotsky A. (2020) Thermodynamics drives the stability of the MOF-74 family in water. ACS Omega 5, 13158–13163.
- Wang D., Yang J., Yan S., Xu J., Chen Y., Pu G. and Luo Y. (2001) A special orogenic-type rare earth element deposit in Maoniuping, Sichuan, China: Geology and geochemistry. *Resour. Geol.* 51, 177–188.
- Wang Z. Y., Fan H. R., Zhou L., Yang K. F. and She H. D. (2020) Carbonatite-related REE deposits: An overview. *Miner.* 10, 965.
- Wilfong R. L., Domingues L. P. and Furlong L. R. (1964) Thermogravimetric analysis of five salts of praseodymium, neodymium, and samarium. J. Am. Ceram. Soc. 47, 240–241.
- Williams-Jones A. E., Migdisov A. and Samson I. M. (2012) Hydrothermal mobilisation of the rare earth elements-a Tale of "Ceria" and "Yttria". *Elements* **8**, 355–360.
- Williams-Jones A. E. and Wood S. A. (1992) A preliminary petrogenetic grid for REE fluorocarbonates and associated minerals. *Geochim. Cosmochim. Acta* **56**, 725–738.
- Winter J. D. (2013) *Principles of Igneous and Metamorphic Petrology*, 2nd ed.,. Pearson.
- Witherspoon P. A. (1991) Geological Problems in Radioactive Waste Isolation: A World Wide Review. U.S. Department of Energy.
- Wood S., Palmer D., Wesolowski D. and Bénézeth P. (2002) The aqueous geochemistry of the rare earth elements and yttrium. Part XI. The solubility of Nd (OH)₃ and hydrolysis of Nd3+ from 30 to 290 C at saturated water vapor pressure with insitu pHm measurement. In Water-Rock Interact. Ore Depos. Environ. Geochemistry A Tribut. to David A. Crerar 229–256.
- Xie Y.-L., Hou Z., Goldfarb R. J., Guo X. and Wang L. (2016) Rare earth element deposits in China. Reviews in Economic Geology 18, 115–136.

- Xiong Y. and Lord A. S. (2008) Experimental investigations of the reaction path in the MgO–CO₂–H₂O system in solutions with various ionic strengths, and their applications to nuclear waste isolation. *Appl. Geochem.* **23**, 1634–1659.
- Xu H., Chavez M. E., Mitchell J. N., Garino T. J., Schwarz H. L., Rodriguez M. A., Rademacher D. X. and Nenoff T. M. (2015) Crystal structure and thermodynamic stability of Ba/Ti-substituted pollucites for radioactive Cs/Ba immobilization ed. L. Vance. J. Am. Ceram. Soc. 98, 2634–2640.
- Xu H., Guo X. and Bai J. (2017) Thermal behavior of polyhalite: a high-temperature synchrotron XRD study. *Phys. Chem. Miner.* 44, 125–135.
- Yang T. F. (2008) Recent progress in the application of gas geochemistry: Examples from Taiwan and the 9th International Gas Geochemistry Conference. *Geofluids* 8, 219–229.
- Yi S. I., Attari V., Jeong M., Jian J., Xue S., Wang H., Arroyave R. and Yu C. (2018) Strain-induced suppression of the miscibility gap in nanostructured Mg₂Si-Mg₂Sn solid solutions. *J. Mater. Chem. A* 6, 17559–17570.
- Zaman M. M. and Antao S. M. (2020) Crystal structure refinements of four monazite samples from different localities. *Miner.* 10, 1028.
- Zhang Y. and Navrotsky A. (2004) Thermochemistry of rare-earth aluminate and aluminosilicate glasses. *J. Non. Cryst. Solids* **341**, 141–151.
- Zhongxin Y., Ge B., Chenyu W., Zhongqin Z. and Xianjiang Y. (1992) Geological features and genesis of the Bayan Obo REE ore deposit, Inner Mongolia, China. Appl. Geochem. 7, 429–442
- Zhou B., Li Z. and Chen C. (2017) Global potential of rare earth resources and rare earth demand from clean technologies. *Minerals* 7, 203.

Guest editor: Fang Xia